

Microstructure-based modelling of snow mechanics: experimental evaluation on the cone penetration test

Clémence Hery^{1,2}, Pascal Hagenmuller¹, Guillaume Chambon², Isabel Peinke¹, Jacques Rouille¹

¹Univ. Grenoble Alpes, Univ. de Toulouse, Météo-France, CNRS, CNRM, Centre d'Etude de la Neige, Grenoble, France

²Univ. Grenoble Alpes, CNRS, INRAE, IRD, Grenoble INP, IGE, Grenoble, France

Correspondence to: Clémence Hery (clemence.hery@gmail.com)

Abstract. Snow is a complex porous material presenting various microstructural patterns. This microstructure largely controls the mechanical properties of snow, and this control still needs, although the relation between the micro and macro properties remains to be better understood. Recent numerical developments based on three-dimensional tomographic data have provided new insights into snow mechanical behaviour. In particular, the discrete element method combined with the snow microstructure captured by tomography (DEM) and the mechanical properties of ice has been used to three-dimensional microtomographic data make it possible to reproduce numerically the brittle mechanical behaviour of snow. However, these developments lack experimental evaluation so far. In this study, we evaluate a DEM numerical model based on the discrete element method with reproducing cone penetration tests on centimetric snow samples. This test is commonly used to characterise the snowpack stratigraphy but also brings into play complex mechanical processes and deformation patterns. We measured the snow microstructure on the microstructures of different natural snow samples were captured with X-ray microtomography before and after the cone penetration test with X-ray tomography. The, from which the grain displacements induced by the cone test was could be inferred. The tests were conducted with the modified Snow MicroPenetrometer (5 mm cone diameter), which recorded the force profile at a high resolution. The initial microstructure and in the ice properties fed the numerical model, which can reproduce the exact same test numerically. We evaluated the model on the measured force profile and the displacement field an elastic brittle cohesive contact law between snow grains was used to represent the cohesive bonds. The initial positions of the grains and their contacts were directly derived from the difference between the initial and final microstructures. The model reasonably tomographic images. The numerical model was evaluated by comparing the measured force profiles and the grain displacement fields. Overall, the model satisfactorily reproduced the force profiles in terms of average mean macroscopic force, force standard deviation, and (mean relative error of about 11%) and the amplitude of force fluctuations (mean relative error of about 21%), while the correlation length of the force fluctuations. When the contact law describing ice mechanics is adjusted in the range of reasonable values for ice, the agreement becomes good on all three parameters. The model also well reproduced was more difficult to reproduce (mean relative error of about 38%). These characteristics were, as expected, highly dependent on the tested sample microstructure, but they were also

Style Definition: Normal
Style Definition: Heading 5
Style Definition: Heading 6
Style Definition: Title
Style Definition: Subtitle

Formatted: French (France)

Formatted: Font colour: Auto, French (France)

Formatted: French (France)

Formatted: French (France)

Formatted: Font colour: Auto

Formatted: Font colour: Auto

Formatted: Font colour: Auto

Formatted: Font colour: Auto

Formatted: Font colour: Auto

Formatted: Font colour: Auto

Formatted: Font colour: Auto

Formatted: Font colour: Auto

Formatted: Font colour: Auto

Formatted: Font colour: Auto

~~sensitive to the choice of the micro-mechanical parameters describing the contact law. A scaling law was proposed between the mechanical parameters, the initial microstructure characteristics and the mean macroscopic force obtained with the DEM numerical model. The model could also reproduce the measured deformation around the cone tip, which is less sensitive (mean grain displacement relative error of about 57% along the horizontal axis), with a smaller sensitivity to the contact law parameterization. Overall, the model is capable of distinguishing the different microstructural patterns tested. Therefore parametrisation in this confrontation of case. These detailed comparisons between numerical results with and experimental measurements for this configuration gives results give confidence in the reliability of the numerical modelling strategy. The model could be further applied with different boundary conditions, and used opens promising prospects to characterise improve the understanding of snow mechanical behaviour of the snow better.~~

Formatted: Font colour: Auto

Formatted: Font colour: Auto

Formatted: Font colour: Auto

1 Introduction

Snow is a brittle and porous material existing on Earth close to its melting point. The thermodynamical conditions in the clouds govern the snowflake morphology and, once deposited on the ground, snow continues to evolve via metamorphism. The snow material is thus characterised by a large variety of microstructural patterns (grain size, grain shape, density) classified into different snow types (Fierz et al., 2009). It has been established that the snow microstructure controls the properties of snow (Shapiro et al., 1997; Johnson and Schneebeli, 1999; Schneebeli, 2004). For instance, weak layers involved in avalanche triggering (Schweizer et al., 2003) are usually constituted of specific snow types (depth hoar, surface hoar, precipitation particle, faceted crystals) characterised by low cohesion and low strength (Jamieson and Johnston, 1992). The link between the snow microstructure and its properties, especially its mechanical properties, is still not well understood, even if it is crucial for many applications, such as ~~for~~ avalanche forecasting (Schweizer et al., 2003, Jamieson and Johnston, 1992), snowpack modelling (Calonne et al. 2014), ice core interpretation (Montagnat et al. 2020) or geotechnics (Shapiro et al., 1997). In particular, the brittle failure occurring at high shear ~~rates~~ ($> 10^{-4} \text{ s}^{-1}$) during the release of an avalanche remains represented by very coarse empirical laws (Brun et al., 1992; Bartelt, et al. 2002; Vionnet et al. 2012) and lacks of relevant microstructural proxies (Shapiro et al., 1997; 2012). In this elastic-brittle regime (rapid and large deformations), the mechanical behaviour of snow is ~~thought to be~~ mainly controlled by bond ~~failure~~ failures and grain rearrangements (Narita, 1983).

The snow microstructure and its evolution can be captured at high resolution (~~tens of micron~~ typically 10-50 μm) with X-ray micro tomography imaging (μCT) (Coléou et al., 2001; Freitag et al., 2004; Schneebeli, 2004; Heggli et al., 2011). This non-destructive method preserves the snow microstructure and resolves the shape of snow grains, grain bonds and porosity which is of primary importance for mechanical studies. In particular structural properties of snow, such as density, specific surface area (SSA), correlation length, bond characteristics, can be evaluated from tomographic data (e.g. Schneebeli, 2004; Schneebeli et al., 2004; Hagenmuller et al., 2014a; Calonne et al., 2014; Proksch et al., 2015). The tomographic data are also used as a basis for numerical modelling (Schneebeli, 2004; Schneebeli et al., 2004; Hagenmuller et al., 2015) or calibration/validation data of statistical empirical models retrieving grain-scale physical and mechanical properties from other

62 measurements (e.g. Proksch et al., 2015; Reuter et al., 2019). However, ~~this method~~tomographic imaging is time-expensive
63 and not adapted to routine measurements in the field.

64 ~~An objective and relatively easy-to-set-up method to measure the~~The mechanical properties of snow ~~is the~~are commonly
65 ~~derived from~~ Cone Penetration Test (CPT) ~~measurements, which is an objective and relatively easy-to-set-up method~~
66 ~~(Schneebeil and Johnson, 1998)~~. This method has been widely used to characterise soil stratigraphy (Lunne et al., 1997) and
67 adapted to snowpack stratigraphy (Gubler, 1975; Schaap and Fohn, 1987; Dowd and Brown, 1986; Schneebeil and Johnson,
68 1998; Mackenzie and Payten, 2002; McCallum, 2014). The CPT provides a force profile by measuring the resisting force
69 exerted on a conic tip penetrating, at a constant rate, into a material. The development of high-resolution digital penetrometers
70 dedicated to snow studies (Schneebeil and Johnson, 1998; Mackenzie and Payten, 2002; McCallum, 2014) ~~have~~has provided
71 the possibility to resolve the force profile at a microscopic scale and capture the high-frequency fluctuations of the force signal
72 up to a metre depth. ~~The~~Such force penetration ~~profile contains~~profiles contain valuable information on the snow structural
73 parameters at macro- and micro-scale (Löwe and van Herwijnen, 2012).

74 Interpretation of the CPT requires a good ~~comprehension~~understanding of the ~~interaction~~interactions between the cone tip and
75 the snow ~~grains and bonds~~. Several studies aimed to investigate the ~~grains~~grain displacement field around the tip. Particle
76 Image Velocimetry (PIV) imaging was performed ~~along on snow~~to quantify the 2D displacement field of snow grains while
77 the tip penetrates ~~into the snow~~material (Floyer and Jamieson, 2010; Herwijnen, 2013; LeBaron et al., 2014). Peinke et al.
78 (2020) developed a grain tracking algorithm to reconstruct from μ CT the 3D displacement field of snow grains ~~due to~~induced
79 ~~by~~ a CPT. All these studies revealed the development of a compaction zone (CZ) in front of the tip ~~that cannot be neglected~~
80 ~~while interpreting force profiles~~.

81 ~~Mechanical~~Various mechanical or statistical models have been developed to interpret the CPT penetration signal in terms of
82 mechanical properties. The cavity expansion model (CEM) (Bishop et al., 1945; Yu and Carter, 2002) ~~is commonly used to~~
83 ~~interpret CPT measurements and~~ has been applied to snow by Ruiz et al. (2016) and Peinke et al. (2020). ~~The CEM~~This model
84 ~~considers snow as a continuum and~~ describes the elastic-plastic deformation of the material around the tip. ~~Macroscopic in~~
85 ~~order to retrieve macroscopic~~ material properties ~~can be retrieved from this model (Ruiz (cohesion, friction, etc.). The~~
86 ~~continuum assumption becomes invalid for a ratio between cone diameter and mean grain diameter lower than 20 typically~~
87 ~~(Bolton et al., 2016; Peinke et al., 2020). The~~ 1993), leading to potentially erroneous interpretations of the CPT results.

88 ~~Alternatively,~~ the shot noise model interprets the force signal and its fluctuations as a superposition of independent elastic–
89 brittle ruptures occurring next to the tip. (Schneebeil and Johnson, 1999; Marshall and Johnson, 2009; Löwe and van Herwijnen,
90 2012;) and retrieves microstructural properties (bond rupture force, etc.) The penetration process is ~~here~~generally modelled
91 ~~by~~as a Homogeneous Poisson Process (HPP) with a constant intensity (Löwe and van Herwijnen, 2012). Peinke et al. (2019)
92 have generalised the HPP method in order to account for the transient statephase of the penetration process, attributed to the
93 development of the CZ (Peinke et al., 2019). ~~They~~These authors used a Non-Homogeneous Poisson Process (NHPP)
94 considering a depth dependency of the intensity, ~~i.e.~~ (number of bond failures per penetration increment. ~~Both models are~~
95 ~~based on different assumptions. First~~). ~~Yet,~~ the CEM considers snow as a continuum, while the HPP considers the discrete

Formatted: Font colour: Auto

Formatted: Font colour: Auto

Formatted: Font colour: Auto

Formatted: Font colour: Auto

Formatted: Font colour: Auto

96 nature of bond failures. The continuum assumption reaches its limit for a cone diameter to mean grain ratio lower than 20
97 (Bolton et al. 1993), leading to a potentially erroneous interpretation of the CPT results. This configuration can be reached for
98 CPT measurements in snow (Herwijnen, 2013; Peinke et al. 2020). Second, the force signal is influenced by the CZ (Herwijnen,
99 2013; LeBaron et al., 2014; Peinke et al. 2020), which is considered in the CEM approach but not in the HPP approach. This
100 may lead to diverging estimations of the absolute value of some macroscopic snow properties (Ruiz et al., 2017). Despite the
101 NHPP can retrieve snow microstructural properties from transient force profiles (Herwijnen, 2013; Peinke et al., 2019), the
102 interpretation of the force profiles, resulting of independent contributions of elastic-brittle failure, neglecting rupture events
103 essentially neglects the development of a CZ remains challenging (Johnson and Schneebeli, 1999; Schneebeli, 2001;
104 Herwijnen, 2013; LeBaron et al., 2014; Ruiz et al. 2017). Therefore, none of these two methods/models appear to fully
105 satisfy/account for the specificity of snow deformation induced by CPT. Additional investigations are required to better
106 understand the tip interaction with snow and the meaning of the derived structural proxies/better interpret the force
107 measurements.

108 The snow properties and its strong dependence on environmental conditions make it difficult to study it experimentally (in the
109 laboratory and in situ) in a systematic and controlled manner. Recently, numerical approaches have been developed to study
110 the mechanical response of snow by explicitly accounting for the microstructure (Johnson and Hopkins, 2005; Gaume et al.,
111 2015, 2017; Hagenmuller et al., 2015; Wautier et al., 2015; Mede et al. 2018b, 2020; Bobillier et al., 2020, 2021). Snow is
112 described as a granular material for which the mechanical behaviour can be and modelled by the discrete element method
113 (DEM) in a high shear rate regime (Hansen and Brown, 1988). The complexity of the snow microstructure can be
114 considered/taken into account by feeding the DEM simulations with high-resolution 3D reconstructions of the snow sample
115 obtained with μ CT. These simulations have provided new insights into the snow mechanical behaviour, such as the dependence
116 of snow strength to microstructure properties (Hagenmuller et al., 2015) or the identification of different failure modes in shear
117 loading (Mede et al., 2018b, 2020). The downside of this method is that it is time-consuming, and simulations can only be
118 performed on small samples (up to a few centimetres). These simulations have nevertheless provided new insights on the snow
119 mechanical behaviour, such as distinct resistance to confined compression for different microstructure properties (Hagenmuller
120 et al., 2015) or identification of failures mode in a mixed mode loading (Mede et al., 2018b, 2020). Although these models
121 appear capable of accounting for the role of the microstructure on the mechanical response, they still lack experimental
122 confrontation. Furthermore, these numerical models still lack direct experimental evaluation.

123 In this context, the aim of this study aimed was to evaluate a microstructure-based DEM model with using recent CPT
124 experimental data of cone penetration tests. To address this goal, we modelled CPT on performed in a realistic
125 representation/controlled environment (Peinke et al., 2020). The dataset includes μ CT images of the snow samples with DEM
126 numerical simulations. The acquired before and after the tests. The deformation induced by the CPT configuration (strain rate
127 of about 10^2 s^{-1} , Reuter et al., 2019) belongs to the elastic-brittle regime (Narita, 1983; Floyer and Jamieson, 2010) and is
128 therefore suitable for DEM simulation. The model has been designed to account for the snow properties and the snow
129 microstructure acquired by μ CT (Hagenmuller et al., 2015; Mede et al., 2018b, 2020). The results of the numerical model are

Formatted: Font colour: Auto

Formatted: Font colour: Auto

Formatted: Font colour: Auto

Formatted: Font colour: Auto

Formatted: Font colour: Auto

Formatted: Font colour: Auto

Formatted: Font colour: Auto

Formatted: Font colour: Auto

130 ~~confronted to results performed experimentally on snow samples (Peinke et al., 2020). We~~ directly compared ~~to experimental~~
131 ~~data in terms of~~ (1) ~~the~~ macroscopic force profile ~~with relevant structural parameters and associated statistical indicators~~ and
132 (2) ~~the~~ grain displacements induced by the cone penetration. A systematic sensitivity analysis to ~~DEM~~ mechanical parameters
133 ~~of the contact law~~, including Young's modulus, ~~the~~ cohesion and ~~the~~ friction ~~angle coefficient~~, was ~~also~~ performed ~~with DEM~~
134 ~~to evaluate their influence on the mechanical behaviour and find the combinations of parameters that best combination of~~
135 ~~mechanical parameters to~~ reproduce experimental results. Finally, the role of the microstructure ~~is was~~ also investigated by
136 performing ~~the~~ DEM simulations ~~with for~~ different snow types. The evaluation of the numerical model provides the opportunity
137 to better understand the mechanisms at ~~workplay~~ during ~~the~~ snow deformation in an elastic-brittle regime and better interpret
138 CPT profiles.

139 We first present the experimental ~~data set dataset~~ and the numerical ~~model used to perform CPT methods~~. The data processing
140 used to compare experimental and numerical results is also explained. The results of the DEM, the sensitivity analysis to
141 mechanical parameters and the comparison to experimental results are then presented. The relevance of the DEM model and
142 the limits of our approach are eventually discussed before concluding.

143 2 Methods

144 2.1 Experiments ~~Experimental measurements~~

145 The experimental ~~data set dataset~~ used in this study has been acquired by Peinke et al. (2020) and is only briefly presented in
146 this paper. The methodology comprises collection and preparation of snow samples, acquisition of high-resolution micro-
147 tomographic images and cone penetration tests (CPT).

148 2.1.1 Snow sample preparation

149 Blocks of natural snow were sampled in the French Alps near Grenoble and stored at -20°C in a cold room. The materials
150 collected ~~are were~~ representative of the variety of seasonal snow types (Table 1), namely rounded grains (RG), large rounded
151 grains (RGl_r), depth hoar (DH) and precipitation particles (PP), with distinct bulk densities and specific surface areas (SSA).

152 The samples were ~~then~~ prepared in a cold room at -10°C by sieving the ~~different~~ snow ~~types~~ into aluminium cylinders, ~~suitable~~
153 ~~for X-ray tomography (high thermal conductivity and relatively low X-ray absorption)~~, of ~~2-cm~~20 mm height and ~~2-cm~~20 mm
154 diameter. All samples were prepared at least 24 hours before the measurements in order for the bonds between grains to rebuild
155 after sieving.

156 2.1.2 Micro-Tomography (μCT)

157 Tomographic scans of each sample were acquired before and after performing the CPT to capture, ~~respectively~~, the initial and
158 final microstructure of the snow, ~~respectively~~. An X-ray tomograph (DeskTom130, RX Solutions) operating at a pixel size of
159 15 μm pix⁻¹, a voltage of 80 kV and a current of 100 μA was used. During tomographic scanning, the samples were maintained

Formatted: Font colour: Auto

160 at a constant and uniform temperature of -10°C in a cryogenic cell (CellDyM, Calonne et al. (2015)). Each scan, consisting of
161 1440 2D radiographs, was reconstructed to obtain 3D grayscale images representing the attenuation coefficients of the different
162 materials composing the samples. The grayscale images were then transformed into binary (ice matrix – pore space) segmented
163 images using an energy-based segmentation algorithm (Hagenmuller et al., 2013).

164 2.1.3 Cone Penetration Test (CPT)

165 ~~Posterior to~~After the initial micro-tomography scan, a CPT was performed on the snow samples using a modified
166 SnowMicroPenetrometer (SMP version 4, Schneebeli and Johnson, 1998). The specific rod used by Peinke et al. (2020)
167 displays a conic tip with an apex angle α of 60° and a maximum cone radius equal to the rod radius R of 2.5 mm. The rod was
168 inserted vertically into the snow sample at a constant penetration speed v of 20 mm s^{-1} . The resisting force applied on the
169 penetrometer (cone and rod) was recorded at every $4\text{ }\mu\text{m}$ of penetration increment (i.e., 5 kHz frequency). The SMP sensor (Kistler
170 sensor type 9207) ~~measures~~can measure forces up to 40 N with a resolution of 0.01 N. The tip was stopped at depths
171 between 7 and 15 mm, i.e., 5- to 13 mm above the sample bottom, to avoid boundary effects (Peinke et al., 2020). The
172 experimental force profiles are presented in Figure S26.

173 2.2 Numerical modelling

174 Snow is here considered as a granular cohesive material. ~~Indeed, the~~The high strain rate ($> 10^{-4}\text{ s}^{-1}$) induced by the tip
175 penetration in the snow sample ~~leads~~is considered to lead to brittle deformations, with inter-granular damage and grain
176 rearrangements (Narita, 1983; Johnson and Hopkins 2005; Hagenmuller et al., 2015). We adopted an approach based on the
177 discrete element method (DEM) to simulate the cone penetration tests in the measured snow samples. The mechanical model
178 is based upon YADE software (Šmilauer et al., 2015), is adapted from the work of Hagenmuller et al. (2015) and Mede et
179 al., (2018a, b and 2019) and is performed with YADE solver (Šmilauer et al., 2015).
180 ~~This modelling approach is composed~~The setting-up of three main the simulations involves different steps, namely the
181 generation of the initial conditions based on the measured snow microstructures, the definition of the contact ~~law~~laws between
182 the snow grains, and the setting of the boundary conditions to reproduce the -CPT configuration.

183 2.2.1 Grain segmentation and grain shape representation

184 The DEM model was fed by the 3D ice-air images ~~obtained with X-ray tomography derived from μCT~~ . The continuous ice
185 matrix was first segmented into individual grains based on geometrical criteria, as described by Hagenmuller et al. (2013).
186 The main idea of the approach is to detect potential mechanical weakness zones (i.e., the bonds) based on the principal minimal
187 curvature κ_T and thea contiguity parameter between the grains c_T . The threshold on curvature κ_T was set at 1.0 for RG, RGlR
188 and DH samples and to 0.7 for PP sample (see Hagenmuller et al., 2013 for details). The; the contiguity parameter was set to
189 0.1 for all the samples (see Hagenmuller et al., (2013) for details).

Formatted: Font colour: Auto

Formatted: Font colour: Auto

Formatted: Font: Not Italic

Formatted: Font colour: Auto

Formatted: Font colour: Auto

Formatted: Font colour: Auto

Formatted: Font: Italic

Formatted: Font: Italic

Formatted: Font: Italic

To construct the DEM sample, the irregular shape of the grains was approximated by filling the grain volume with a population of overlapping spheres (Fig. 1). The position of these spheres were derived from the medial axis of the structure (Coeurjolly and Montanvert, 2017; Mede et al., 2018a) and redundant spheres were discarded based on a power diagram filter (Coeurjolly et al., 2007; Montanvert, 2017). This grain shape representation by a multitude of spheres preserves the capability of YADE to handle sphere-sphere contact detection. However, a high number of spheres slows the numerical simulation down the simulations. We thus further decimated the number of spheres by approximating the grain volume shape. We only selected the spheres with a radius larger than a threshold L (voxel) and covering (in the sense of with a relative coverage larger than S (i.e., the ice volume associated with the sphere according to the power diagram) a large proportion of the grain should be larger than S times the sphere volume (parameter S ; Coeurjolly et al., 2007). A trade-off must be found between the error of this grain shape approximation, influencing the mechanical behaviour simulation accuracy, and the number of spheres influencing the numerical cost of the simulations. Eventually, the spheres belonging to the same grain were clumped together in rigid aggregates constituting single discrete elements (DE). A detailed sensitivity analysis to this grain representation was conducted (see supplementary material, Table S1, and Fig. S1) to determine the optimal R values of L and S parameters. Note that this grain shape approximation might also lead to delete the smallest grains in the numerical samples, as they cannot be covered with the chosen R parameters L and S . The grain number difference and shape approximation of the numerical sample compared to initial the segmented μ CT image can be quantified by computing the volumetric error E_V . The final chosen L and S values for each snow type, with the associated with the volumetric E_V and mechanical E_M errors, (defined in Sect. S1.1), can be found in Table 1. Eventually, the spheres belonging to the same grain were clumped together in rigid aggregate and constitute a single discrete element (DE).

Sample name	Snow type	Sieve size (mm)	Bulk density (kg m ⁻³)	SSA (m ² kg ⁻¹)	R L (vx)	S	Number of spheres	Number of clumps/grains	Number of initial cohesive interactions between clumps/grains	Initial contact density ν	E_V (%)	E_M (%)
RG	Rounded Grains	1.6	289	23.0	5	0.3	514917	27560	47736	0.55	42.3	18.9 5.3
RGlr	Large Rounded Grains	1	530	10.1	5	0.3	270143	8488	24005	1.63	14.6	94.2
DH	Depth Hoar	1.6	364	15.9	5	0.2	743546	11211	24258	0.86	24.7	12.7 14.3
PP	Precipitation Particle	1.6	91.3	53.5	2	0.5	1797567	95022	125805	0.13	32.2	9.6 0.3

Table 1: Overview of the snow samples analysed in this study and the respective parameters of DEM grain shape representation chosen. The sample, Sample names were given according to the snow type classification (Fierz et al., 2009). The sample density and

Formatted: Font colour: Auto

Formatted: Font colour: Auto

Formatted: Font colour: Auto

Formatted: Font colour: Auto

Formatted: Font colour: Auto

Formatted: Font colour: Auto

Formatted: Font colour: Auto

Formatted: Font colour: Auto

Formatted: Font colour: Auto

Formatted: Font colour: Auto

Formatted: Font colour: Auto

Formatted: Font colour: Auto

Formatted: Font colour: Auto

Formatted: Font colour: Auto

Formatted: Font colour: Auto

Formatted: Font colour: Auto

Formatted: Font colour: Auto

Formatted: Font colour: Auto

Formatted: Font colour: Auto

Formatted: Font colour: Auto

Formatted: Font colour: Auto

Formatted: Font colour: Auto

Formatted: Font colour: Auto

Formatted: Font colour: Auto

Formatted: Font colour: Auto

Formatted: Font colour: Auto

Formatted: Font colour: Auto

Formatted: Font colour: Auto

Formatted: Font colour: Auto

Formatted: Font colour: Auto

Formatted: Font colour: Auto

Formatted: Font colour: Auto

Formatted: Font colour: Auto

Formatted: Font colour: Auto

Formatted: Font colour: Auto

Formatted: Font colour: Auto

Formatted: Font colour: Auto

Inserted Cells

specific surface area (SSA) were derived from the micro-tomographic images (Peinke et al., 2020). The initial contact density was computed according to Eq. 10. The minimum radius of the sphere R_L and the minimum sphere coverage S were determined by through a sensitivity analysis presented in Sect. S1.1. The associated resulting number of spheres, grains and cohesive grain-grain interaction interactions are indicated. Finally, as well as the volumetric error E_V and the mechanical error E_M for associated with each grain shape representation were calculated.

2.2.2 Interactions and contact law

The contacts between adjacent grains were identified during the grain segmentation phase. In the DEM simulations, the each grain contacts were contact is represented by several sphere-sphere interactions. The interactions between spheres were are described by an elastic brittle cohesive contact law. The adhesion A , Eq. (1), characterised by four parameters, namely the normal contact stiffness K_N , Eq. (2) and the shear contact stiffness K_S and K_C , Eq. (3) were initially set the adhesion A , and the friction angle φ . The normal force F_N between two spheres is computed as: proportional to the distance between the two sphere surfaces x_N , and limited by the adhesion value in the tensile regime ($x_N > 0$);

$$F_N A = D \times C, \quad = K_N x_N \leq A, \quad (1)$$

$$K_N = \frac{D \times E}{r_{\text{mean}}^3}, \quad (2)$$

$$\text{The shear force } F_S = \nu \times K_N, \quad (3)$$

with D the contact area between two spheres (m^2), weighting the bond magnitude between grains according to the spheres size, C the cohesion (Pa) of ice, E Young's modulus (Pa) of ice, r_{mean} (mm) the mean sphere radius of the numerical sample, which constitute a characteristic length of the grain shape representation of the sample and is used to scale the normal stiffness in order that all the sphere-sphere interactions between two grains fails at the same moment, and finally, ν the Poisson's ratio of the material.

The forces acting on the spheres in contact depend on the stiffness of the material (Mede et al., 2020). The tensile force F_N , Eq. (4) is proportional to the distance between two considered spheres x_N :

$$\text{shear } F_S = K_N x_N \leq A, \quad (4)$$

The contact between spheres exists as long as F_N remains below the adhesion value A . Once the cohesion is broken in tension, the bond is not cohesive anymore also in the shear direction. The shear force F_S , Eq. (5), display a linear dependency to the relative displacement of the sphere to the considered neighbouring sphere between the spheres x_S , with a maximal shear force limited value given by the sum of adhesion and Mohr-Coulomb friction:

$$F_S = K_S x_S \leq A + F_N \times \tan \varphi, \quad (5)$$

Formatted: Font: Italic

Formatted: Font colour: Auto

Formatted: Font: Italic

Formatted: Font: Italic

Formatted: Font colour: Auto

Formatted: Font colour: Auto

Formatted: Font: Italic, Font colour: Auto

Formatted: Font colour: Auto

Formatted: Font colour: Auto

Formatted: Font colour: Auto

Formatted: Font: Italic

Formatted: Font colour: Auto

Formatted: Font: Italic

Formatted: Space Before: 6 pt, After: 6 pt

Formatted: Font colour: Auto

Formatted: Font: Italic, Font colour: Auto

Formatted: Font colour: Auto

Formatted: Font colour: Auto

Formatted: Font colour: Auto

Formatted: Font: Italic

Formatted: Font: Italic

Formatted: Font: Italic

244 where ϕ is the friction angle. If the force exceeds the threshold, either in tension or in shear, the cohesive bond is broken. As
245 long as the spheres remain in contact after the cohesion has been bond is broken, Mohr-Coulomb friction remains active in
246 shear.

247 The contact force, stiffness and adhesion of grains in contact correspond to the sum of the respective values of all the spheres
248 in contact. At In the initial step of the simulation, all contacts state, all interactions in the numerical sample are considered
249 cohesive. While the numerical sample deforms, new clumps positions are computed with the momentum conservation
250 equation. Grain motion can potentially grain displacements lead to progressive breakage of the initial cohesive interactions
251 failure and the potential creation of new contacts. These new interactions. New interactions created during the computation
252 are frictional only (no cohesion), meaning that sintering mechanisms are not considered in this study.

253 The force of a given intergranular cohesive contact corresponds to the sum of all the associated sphere-sphere interactions.
254 Based on the total contact surface between two grains (obtained from the μ CT image) and the number of associated sphere-
255 sphere interactions, each sphere-sphere interaction i can be associated with a representative contact surface D_i . In order to
256 recover the correct cohesion strength between two grains, the adhesion parameter A was defined for each sphere-sphere
257 interaction as:

$$258 A_i = D_i C, \quad (3)$$

259 with C (Pa) the cohesion of ice. In YADE, by default, the contact stiffnesses are computed based on the radii of the spheres in
260 interaction and two elastic material parameters, namely the Young's modulus E and the Poisson ratio ν . For our computations,
261 to ensure that all cohesive sphere-sphere interactions between two grains break at the same separation distance, the computation
262 of the normal stiffness was redefined as:

$$263 K_{N,i} = \frac{D_i E}{r_{mean}}, \quad (4)$$

264 where r_{mean} (m) is a characteristic length constant for all the interactions in the numerical sample, taken as the mean sphere
265 radius. The shear stiffness is then defined as:

$$266 K_S = \nu \times K_N. \quad (5)$$

267 Note that due to the rather arbitrary characteristic length considered in the definition of the normal stiffness [Eq. (4)], which
268 depends on the grain shape approximation, as well as to the simple linear relation considered for the normal force [Eq. (1)],
269 the contact-level YADE Young's modulus E should not be regarded as the "true" Young's modulus of the material, but rather
270 as a representative parameter of the elastic properties at the contacts.

271

Formatted: Font colour: Auto

Formatted: Font colour: Auto

Formatted: Font colour: Auto

Formatted: Font colour: Auto

Formatted: Font colour: Auto

Formatted: Font colour: Auto

Formatted: Font colour: Auto

Formatted: Font colour: Auto

Formatted: Font colour: Auto

Formatted: Font colour: Auto

Formatted: Font colour: Auto

Formatted: Font colour: Auto

Formatted: Font colour: Auto

Formatted: Font colour: Auto

2.2.3 ~~Boundary conditions~~Simulation setup and critical time step

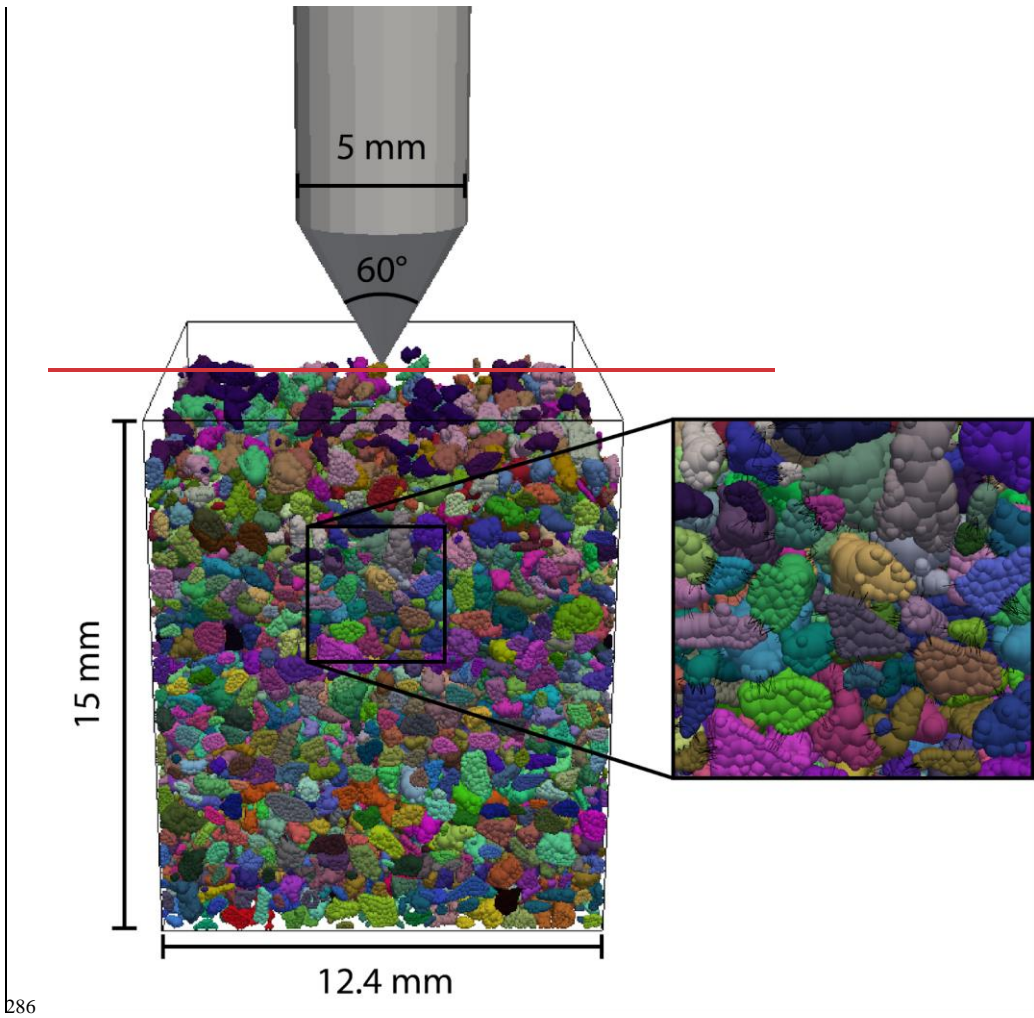
In order to evaluate the DEM model, we have implemented a CPT configuration similar to the experimental ~~set-up~~setup used by Peinke et al. (2020) (Fig. 1). The snow sample is contained in a rectangular box ~~opened~~open at the top. The box ~~displays the following dimensions, is~~ about 12.4 mm along the x - and y -axis and about 15 mm along the z -axis. The ~~box size along the vertical and horizontal plane. It has been~~box sizes were reduced compared to the 20 mm ~~height and 20 mm diameter respectively~~ of the sample holder used by Peinke et al. (2020). This choice has been motivated ~~first to simplify by (1) simplifying the geometry with a rectangular numerical sample, (2) matching the sample height imaged with μ CT, and second to reduce the number of spheres decreasing~~(3) ~~reducing~~ the computational time. A sample size sensitivity analysis has been performed to ensure ~~that~~ border effects are not introduced by reducing the sample size (Fig. S2). The ~~penetrometer~~ tip displays a maximal radius r of 2.5 mm and an apex angle α of 60° . ~~The tip, initially~~Initially in a ~~centred~~centered position at the box surface, ~~it is travelling downward, displaced downwards~~ through the sample, at a constant speed of 20 mm s^{-1} . The simulation stops when the tip reaches the bottom of the box. The walls (box and tip) are represented by facets with rigid boundary conditions. The gravity is set to 9.81 m s^{-2} .

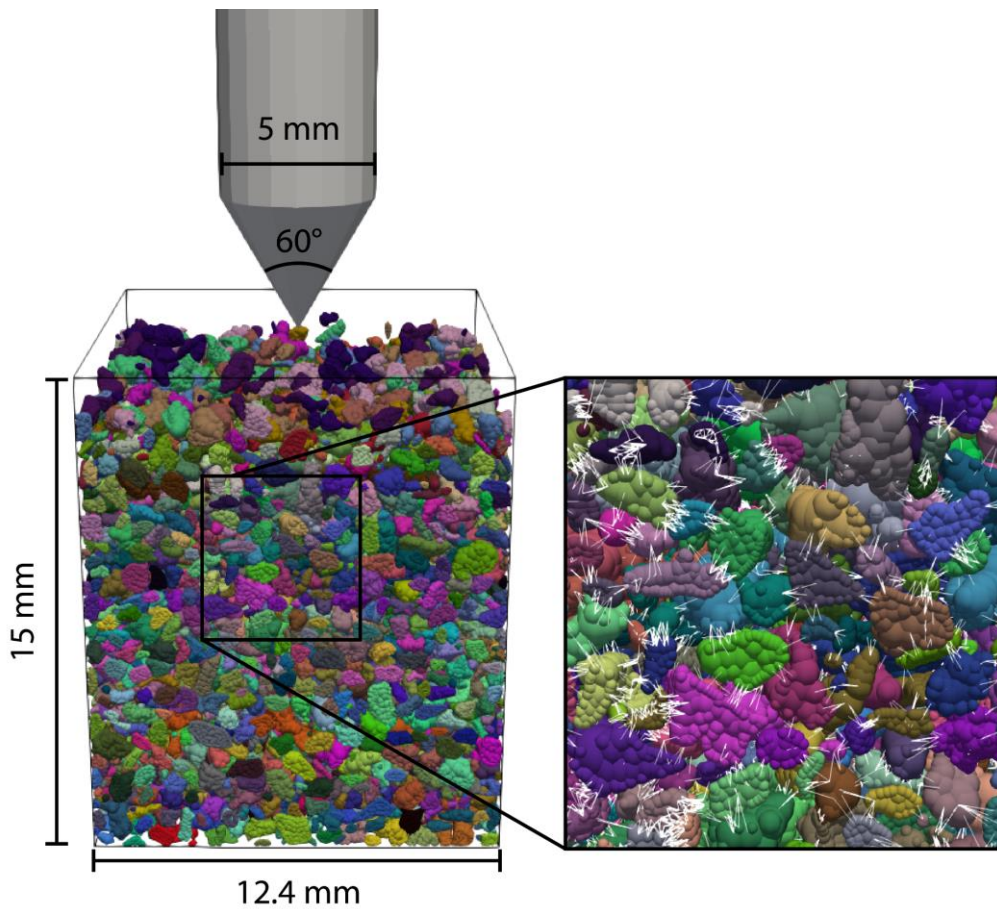
Formatted: Font colour: Auto

Formatted: Font colour: Auto

Formatted: Font: Arial, 12 pt

Formatted: Border: Top: (No border), Bottom: (No border), Left: (No border), Right: (No border), Between : (No border)





287
 288 **Figure 1: Visualisation of DEM CPT modelling with DEM model for the RGl_r sample. The tippenrometer is**
 289 **travelling moving downward at a constant speed of 20 mm s⁻¹. Grains Snow grains (represented with different colours) are composed**
 290 **of modelled by overlapping spheres clumped together (single colour). The zoomed window focuses on DEM grains. Black lines**
 291 **correspond to shows the initial cohesive interactions between the spheres of adjacent grains. (white lines).**

Formatted: Font colour: Auto

292
 293 The stability of the explicit integration scheme of the continuum equations is ensured by estimating the critical time step, Eq.
 294 (6) based on the propagation speed of elastic waves in the sample (Zhao, 2017):

$$\Delta t_{cr} = \min \left(\frac{m_i}{K_{N,i}} \right)^{0.5}, \quad (6)$$

with m_i and $K_{N,i}$ the mass and normal stiffness of the discrete element i . The grain-mass m_i or, equivalently the material density ρ_s , can be artificially increased to increase the time step (Hagenmuller et al., 2015). A numerical sensitivity analysis (Fig. S3) has shown that increasing the mass density by a factor f equal to 100 does not affect the simulation results, while significantly reducing the computing time. Finally, a Cundall's non-viscous damping coefficient λ was applied to the particle acceleration to dissipate kinetic energy and avoid numerical instabilities (Šmilauer et al. 2015). A value of 0.05 was applied chosen according to the results of a numerical sensitivity analysis (Fig. S4).

2.2.4 Input parameters

In view of the preceding paragraph, the density of the ice grains was set to $\rho = f \times 917 \text{ kg m}^{-3}$. The contact law parameters were derived from typical values measured on ice. The Poisson coefficient ν was set to 0.3 (Schulson and Duval, 2009). The typical Young's modulus E , the cohesion strength C and the friction angle coefficient $\tan(\phi)$ values for the ice are usually evaluated respectively around $1 \times 10^{10} \text{ Pa}$, $1 \times 10^6 \text{ Pa}$ and 0.2, respectively (Gammon et al., 1983; Schulson and Duval, 2009). For this study, we performed a sensitivity analysis of the simulation to the values of these parameters was performed to get insights into the model behaviour. The mechanical parameters were either directly derived from the values obtained on ice or adjusted to fit their influence and best adjust simulation results to the experimental measurements. We performed the analysis over the considered ranges of E $1 \times 10^8 - 1 \times 10^{10} \text{ Pa}$ for E , $5 \times 10^5 - 5 \times 10^6 \text{ Pa}$ for C and 0.2-0.5 for $\tan(\phi)$, respectively. Note that the range of Young's modulus E ensures small grain overlap, which satisfies overlaps, i.e. compliance with the rigid grain assumption (Fig. S5). We must mention that, due to longer computing times, fewer parameter values could be explored for large Young's modulus values. For the PP sample, no numerical simulations could be performed for a Young's modulus of $1 \times 10^{10} \text{ Pa}$, as computing times were unreasonable ($E = 1 \times 10^8 \text{ Pa}$, $t \sim 4$ months and $E = 1 \times 10^9 \text{ Pa}$, $t \sim 10$ months on a 72 cores machine with 2.6 GHz Intel Xeon processors (2.6 GHz) and 500 GB RAM. YADE scripts enable parallelisation on up to 5 cores).

Boundary conditions		
Sample width	W	13 mm
Sample height	H	15 mm
Tip radius	R	2.5 mm
Cone apex	α	60°
Tip velocity	v	20 mm s ⁻¹
Gravity	g	9.81 m s ⁻²
Numerical parameters		
Time step	dt	$\sim 1 \times 10^{-6} - 1 \times 10^{-8} \text{ s}$
Mass factor	f	100
Non-viscous damping coefficient	λ	0.05
Material properties		
Grain density	ρ_s	$917 \times 10^2 \text{ kg m}^{-3}$

Formatted: Font: Italic

Formatted: Font: Italic

Formatted: Font: Italic

Formatted: Font: Italic

Formatted: Font: Italic

Formatted: Font colour: Auto

Formatted: Font: Italic

Formatted: Font: Italic

Formatted: Font: Italic

Formatted: Font: Italic

Formatted: Font: Italic

Formatted: Font: Italic

Formatted: Font colour: Auto

Formatted: Font colour: Auto

Formatted: Font colour: Auto

Formatted: Font: Italic

Formatted: Font: Italic

Formatted: Font: Italic

Formatted: Font: Italic

Formatted Table

Formatted: Font: Italic

Formatted: Font: Italic

Formatted Table

Formatted: Font: Italic, Font colour: Auto

Formatted: Font: Italic

Formatted: Font: Italic, Font colour: Auto

Formatted: Font: Italic

Formatted: Font: Italic

Formatted: Font: Italic

Formatted: Font: Italic

Formatted: Font: Italic

Formatted: Font: Italic

Poisson coefficient	ν	0.3
Friction angle coefficient	$\tan(\varphi)$	0.2–0.5 (default value 0.2)
Young's modulus	E	1×10^8 – 1×10^{10} (default value 1×10^9) Pa
Cohesion	C	5×10^5 – 5×10^6 (default value 1×10^6) Pa

Table 2: Input parameters used for the simulations presented in this paper.

2.3 Data processing

The main outputs of the DEM simulations are the resisting force exerted by the grains on the penetrometer penetrating rod and the displacement of the grains induced by the cone penetration. These results can be directly compared to the experimental measurements to evaluate the DEM model.

2.3.1 Force sampling

The sum of the forces along the z-axis applied on all the facets constituting the penetrometer (cone and rod) is recorded at each time step. The characteristics of the SMP (i.e., 4 μm), the numerical force profiles depend on the numerical parameters (notably the time step), and are not necessarily suited for direct comparison with experimental results. To obtain numerical profiles that can be compared to their experimental counterparts, the simulated force values were averaged over windows corresponding to displacement increments of 4 μm , thus matching the sampling frequency of the SMP. This smoothing is also useful to avoid smooth out high-frequency fluctuations linked to the very small time steps used in DEM. Finally, numerical and experimental force profiles are then re-sampled by linear interpolation over a regular grid with a step of 4 μm over the same depth. The profiles span from a depth of 0 mm (initial contact between the cone and the sample surface) to the chosen maximum depth, which, in our study, is set to 7 mm (i.e., 1750 points). This value corresponds to the minimum depth reached by the penetrometer during the experimental CPT tests for the selected samples.

2.3.2 Statistical indicators

Quantitatively, the DEM numerical model is evaluated by a comparison with experimental force profiles, in terms of three statistical indicators: the mean macroscopic force F_z (N), the standard deviation σ amplitude of the force fluctuations, σ (N), and the correlation length l_c (mm). The standard deviation indicator σ is calculated on a as the variance of the detrended force profile obtained by subtracting the mean force values as follows:

$$\sigma = \sqrt{\overline{\tilde{F}^2}}, \quad \tilde{F} = \frac{F - F_{sm}}{F_{sm}} \quad (7)$$

with \tilde{F} (Eq. (5)), Peinke et al. 2019), the detrended force profile, F , the force profile and F_{sm} , the averaged force profile calculated over a rolling window $\Delta z = 3$ mm, to take only into account the force fluctuations and not the global trend of the profile. The correlation length l_c (mm) is also computed on the detrended force profiles-profile (Peinke et al. 2019). In our

Formatted: Font: Italic

Formatted: Font: Italic

Formatted: Font: Italic

Formatted: Font: Italic

Formatted: Font colour: Auto

Formatted: Font colour: Auto

Formatted: Font colour: Auto

Formatted: Font: +Body (Times New Roman)

Formatted: Font: +Body (Times New Roman)

Formatted: Font: +Body (Times New Roman)

Formatted: Font: +Body (Times New Roman)

Formatted: Font: +Body (Times New Roman)

Formatted: Font colour: Auto

Formatted: Font: Italic

Formatted: Font colour: Auto

Formatted: Font: Italic

Formatted: Font colour: Auto

Formatted: Font: Italic, Font colour: Auto

Formatted: Font colour: Auto

Formatted: Font: Italic

study, the snow samples exhibit a rather homogeneous structure allowing us to consider ~~that/ is~~ constant over ~~the~~ depth (Peinke et al., 2019). These three statistical indicators have been chosen because they are easily quantifiable and commonly used to describe force profiles obtained by CPT in snow (Johnsson and Schneebeli, 1999; Löwe and van Herwijnen, 2012; Peinke et al. 2019). ~~They~~In addition, ~~they~~ constitute key parameters to derive additional microstructural properties based on Poisson shot noise models (Löwe and van Herwijnen, 2012; Peinke et al. 2019).

To select the set of ~~model~~ mechanical parameters (E , C and $\tan(\phi)$) providing the best fit to the experimental measurements among the tested values (Table 2), the total, a global error RE_{tot} is computed as the root square of the addition according to:

$$RE_{tot} = \sqrt{2 RE_F^2 + RE_\sigma^2 + RE_l^2} \quad (8)$$

with RE_k the relative error calculated for the three statistical indicators, $k = (F, \sigma, l)$, as:

$$RE_k = \frac{\log(\text{measured value}_k - \text{computed value}_k)}{\log(\text{measured value}_k)} \quad (9)$$

Given the difficulties in reproducing the correlation length with the DEM model for two out of four samples and the fact that the values of the squared statistical indicators vary over several orders of magnitude (see Section 3.2), the relative errors of the structural parameters obtained with numerical modelling compared to the ones obtained for experimental measurements- RE_k were computed with the log of the considered values. We ~~attribute~~have attributed a weight factor of 2 to the relative error RE_F related to the mean macroscopic force relative error as we assume it is the main parameter to reproduce. The-, to put more emphasis on the correct reproduction of this quantity. Hence, for each snow sample, the set of mechanical parameters ~~for which~~ the lowest value of total error is obtained, is considered as the most representative of the physical characteristics of the different types of snow samples. ~~minimising the total error RE_{tot} was determined.~~

2.3.3 Grain displacement analysis

The ~~grain~~ position ~~is~~of all grains was recorded every ~0.4 mm of penetration in the DEM simulations. The total displacement~~displacements~~ and the ~~displacement path~~trajectories can therefore be reconstructed for each grain. Due to the thermodynamically active nature of the snow, ~~the incremental record of the snow sample state during the interrupted experimental CPT wastests were not possible. Therefore we~~feasible and only measured the initial (before CPT) and the final ~~state~~states (after CPT) of the snow sample ~~could be imaged by μ CT~~. Grain tracking, applied to the micro-tomographic images, has been performed by Peinke et al. (2020), providing the total displacement of the identified grains. We ~~thus~~ compared the total displacement between the CPT experiments and the DEM simulations at the same penetration depth, i.e., at the maximal penetration measured experimentally. ~~Note that grain tracking could not be performed for the PP sample due to the small size of the grains.~~

The profiles of vertical and radial displacements were averaged around the cone axis and ~~on~~over the height of an area located between the top section of the cone and the sample surface. A displacement threshold of 0.03 mm ~~is~~was set to define the ~~deformation zone (DZ)~~CZ (Peinke et al., 2020). Only the radial profiles were compared to the experimental results, as we suspect the vertical profiles derived from μ CT scans might be misleading (Peinke et al. 2020). Indeed, before acquiring the

Formatted: Font: Italic

Formatted: Font colour: Auto

Formatted: Font: Italic

Formatted: Font: Italic

Formatted: Font: Italic

Formatted: Font colour: Auto

Formatted: Font colour: Auto

Formatted: Font colour: Auto

Formatted: Font colour: Auto

Formatted: Font colour: Auto

Formatted: Font colour: Auto

Formatted: Font colour: Auto

Formatted: Font colour: Auto

Formatted: Font colour: Auto

377 post-CPT μ CT scans, the tip was removed from the snow. This procedure ~~is~~was performed about one hour after the tip
378 penetration ~~in order, to allow~~ for the bonds between ice grains to ~~re~~-form by sintering ~~to~~and limit the grains displacement while
379 the grain displacements during tip ~~is~~ removed. ~~Despite~~removal. However, despite this precaution, some grains in contact with
380 the tip might ~~behave been~~ dragged upward due to the tip-grain friction, with the tip. Therefore, the grain trajectory observed
381 on the pre- and post-CPT μ CT scans could enhance the upward component of the vertical displacement ~~for~~might have been
382 overestimated in the experimental results, especially for the larger grains.

Formatted: Font colour: Auto

383 3 Results

384 3.1 Simulated Cone Penetration Tests on numerical samples with DEM

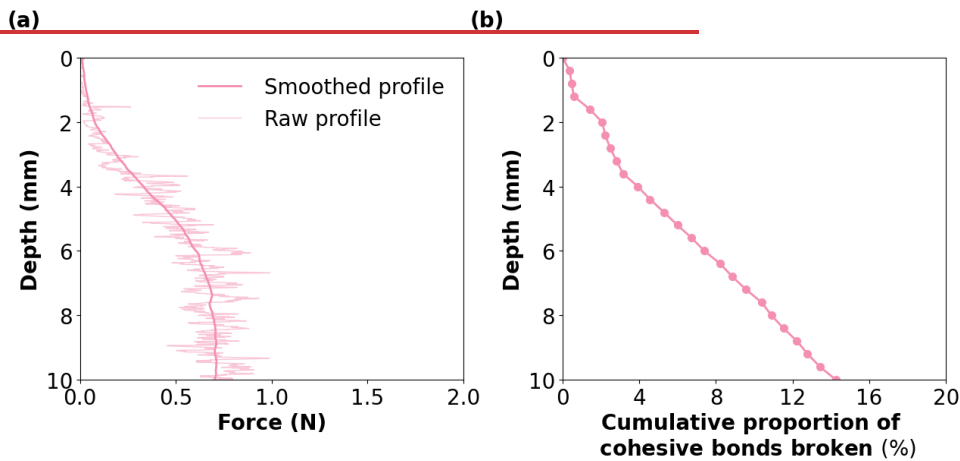
385 This section ~~shows~~presents an example of CPT simulation results obtained for a DEM simulation the case of the CPT on the
386 numerical RG snow sample RG with the following mechanical parameters: $E = 1 \times 10^9$ Pa, $C = 5 \times 10^6$ Pa and $\tan(\phi) = 0.2$
387 (Table 3). The results for the other snow samples are shown in [Seet.Section](#) S2.1.

Formatted: Font: Italic

Formatted: Font: Italic

Formatted: Font: Italic

Formatted: Font: Arial, 12 pt, Font colour: Auto



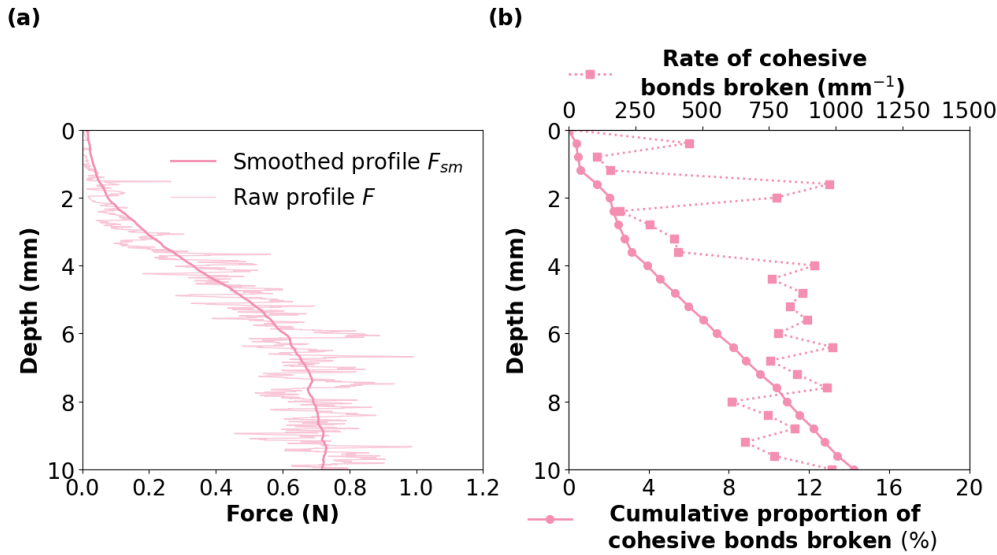


Figure 2: (a) Force F as a function of penetration depth (light line) obtained for the RG sample. The superposed smoothed profile (bold line) F_{sm} corresponds to the averaged force value averaged over a rolling window of 3 mm. (b) Cumulative percentage Rate of cohesive bonds broken as per unit penetration depth and cumulative proportion of cohesive bonds broken (%) as a function of tip penetration depth. The initial number of cohesive bonds is indicated in Table 1. Results The results are obtained with the mechanical parameters given indicated in Table 3.

The simulated penetration force globally increases with depth, with and is characterised by high-frequency fluctuations whose amplitude also tends to increase with depth (Fig. 2 (a)). The force profile displays an 'S' shape with three stages: 1) up to ~ 3.5 mm depth, the profile is convex, 2) between ~ 3.5 and ~ 6 mm depth, the increase of force with depth is almost linear, and 3) for depths larger than 6 mm, the force reaches a nearly constant value. A similar behaviour is observable for all the RGIr and PP samples (Figs Fig. S6 (a), S8 (a), and S10 (a)), with slight changes/variations in the transition depths between the different stages. For the DH sample, the macroscopic force profile also displays stages 1 and 2, but the stabilisation at a nearly constant value is less evident for the results presented in Fig. S (a). Stage 3 might be reached at greater depths for this sample. The penetration of the tip induces bond failures in the simulated samples. The number of bond failures globally increases at a constant rate with penetration depth (Fig. 2 (b)). Overall, for the RG sample, about 15% of the cohesive interactions broke over 10 mm of penetration, corresponding to an average rate of ~710/650 bond failures mm^{-1} . This average bond failure rate is variable among the samples, reaching ~200 up to 1400 bond failure/failures mm^{-1} for RGIr sample (Figs. S6 (b), S8 (b), S10 (b)). In detail, for the RG sample, we notice an increase of in the bond failure intensity/rate at around 3.5 mm of penetration depth (Fig. 2 (b)), coinciding with the transition between the first and second stages observed in the force signal (Fig. 2 (a)).

Formatted: Font: Italic

Formatted: Font: 10 pt, Not Bold, Font colour: Auto

Formatted: Font colour: Auto

Formatted: Font colour: Auto

Formatted: Font colour: Auto

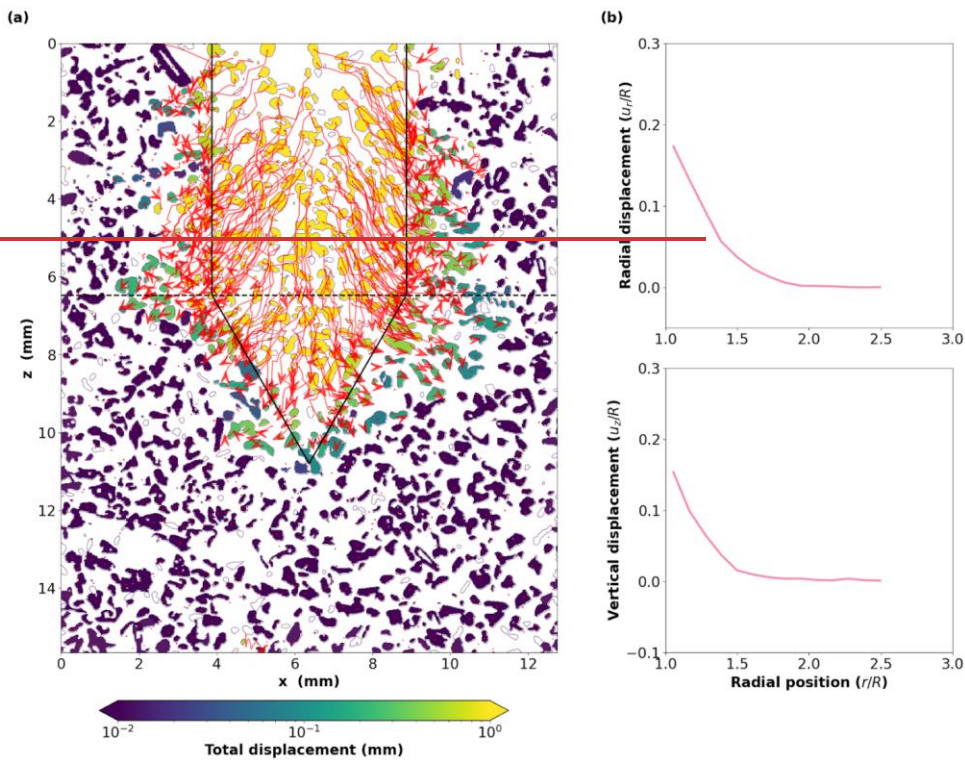
Formatted: Font colour: Auto

411 Bond failure intensity then remains unchangednearly constant as the macroscopic force reaches its steady-state value. Similar
412 characteristics are observed for the other snow types (Figs. S6, S8, S10), S6, S10 except for the DH sample, for which the
413 slope change between the first and second stages is less clear (Fig. S8 (b)).

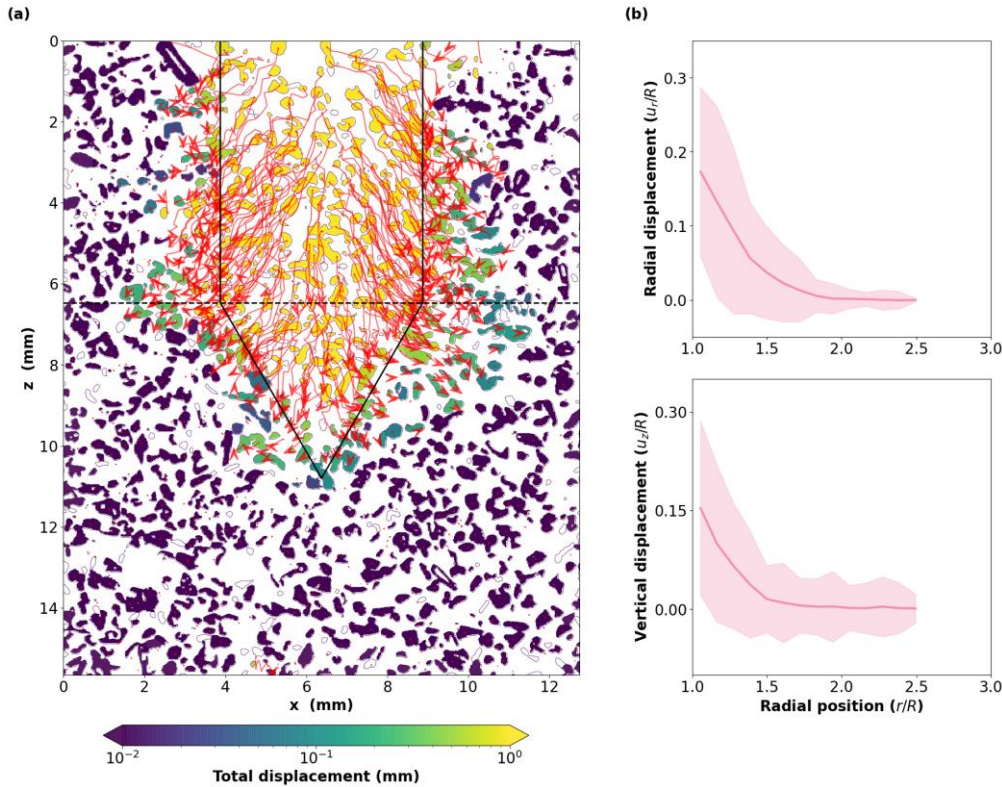
414

Formatted: Font: Arial, 12 pt

Formatted: Space After: 10 pt



415



416
 417 Figure 3: (a) Simulated grain displacement map for the RG sample. The red arrows indicate the grain trajectories while the tip is
 418 penetrating (sampling = 0.4 mm). White grains correspond to grains that are not represented in the DEM simulation. The final tip
 419 position is indicated by the black solid lines. The horizontal black dashed line indicates the cone top. (b) Radial (upper panel) and
 420 vertical (lower panel) displacement profiles (red curves) for the RG sample. These profiles represent averages computed from the
 421 sample surface to the cone top. By convention, downward (respectively upward) movement corresponds to positive (respectively
 422 negative) values of vertical displacement. Results The shadowed areas around the solid lines represent the standard deviation of
 423 grain displacements. The results are obtained with the mechanical parameters given indicated in Table 3.

424
 425 DEM simulations also allow tracking grain positions while the tip is penetrating into the numerical sample. Figure 3a-3 (a)
 426 shows the total displacement of the grains and their respective as well as grain trajectories for the RG sample. The largest
 427 displacements (up to several mm) are observed for grains initially located on the trajectory path of the tip. Around the tip,
 428 the displacements are < 1 mm and are mainly localised close to the tip. Grain trajectories indicate that grains are pushed downward

Formatted: Font colour: Auto

429 from each side of the tip. Grains initially located on the ~~penetrometer tip~~ axis display ~~a~~-quasi-straight vertical
 430 ~~trajectory~~trajectories. The trajectories become more radial and curved away from the tip medial axis, with ~~the~~ grains ~~also~~
 431 being ~~also~~ pushed aside. ~~Around the cone, grain trajectories are predominantly straight, with an almost radial orientation at the~~
 432 ~~cone top and a more vertical orientation near the tip.~~ Both radial and vertical displacement profiles show a pronounced
 433 decreasing trend, and reach ~~almost zero~~ values at a radial position of about ~~1.7R-1.8R~~ (Fig. 3 (b)). The vertical profile attests
 434 of a dominant downward movement of the grains close to the tip. Similar observations are made for the DH ~~sample~~ (Fig. S9) ~~and~~
 435 ~~and~~ PP (Fig. S11) samples. In contrast, for the RGr sample, vertical displacements are smaller and oriented slightly
 436 ~~upwards~~upward on average, for the mechanical parameters chosen here (Fig. S7).

437 **3.2 Sensitivity to mechanical parameters**

438 The influence of the mechanical parameters (Young's modulus, cohesion, friction ~~angle~~-describingcoefficient) involved in
 439 the contact law, ~~on the simulations~~ has been systematically explored. ~~The~~For the RG sample, the force profiles obtained for
 440 the different values of the parameters within the explored ranges (Table 2) are presented ~~for the RG sample~~ in Figure 4, and a
 441 synthetic ~~plot~~plots of the sensitivity of the statistical indicators to these parameters ~~is~~are presented in Figure 5. The results for
 442 ~~the other snow samples as well as can be found in Sect. S2.3, Table S2 summarising all S3 also summarises the values of~~
 443 ~~statistical indicators obtained, can be found in Sect. S2.3 in all cases.~~

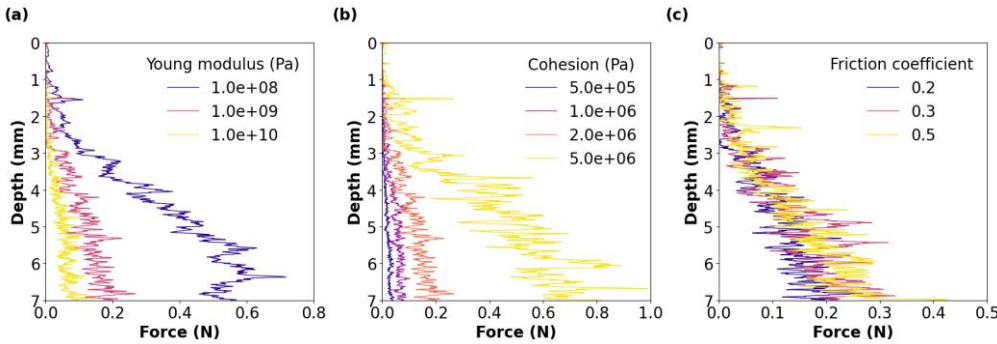
Formatted: Font colour: Auto

Formatted: Font colour: Auto

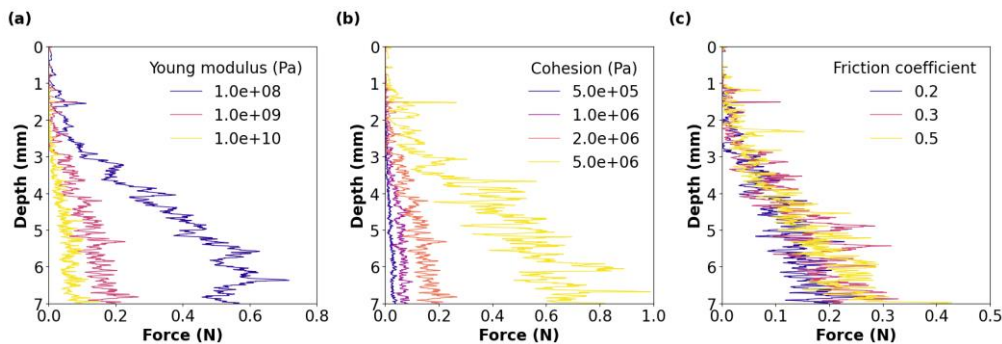
Formatted: Font colour: Auto

Formatted: Font colour: Auto

Formatted: Font colour: Auto



445



446 Figure 4: Influence of mechanical parameters on the simulated force profile. The sensitivity analysis has been performed on (a)
 447 Young's modulus E (Pa) (for $C = 2.0 \times 10^6$ Pa and $\tan(\phi) = 0.2$), (b) the cohesion C (Pa) (for $E = 1.0 \times 10^9$ Pa and $\tan(\phi) = 0.2$), and
 448 (c) the friction coefficient $\tan(\phi)$ (for $E = 1.0 \times 10^9$ Pa and $C = 2.0 \times 10^6$ Pa). Results The results presented here correspond to the RG
 449 sample.
 450

451 First, we observe it can be observed that increasing Young's modulus decreases the mean macroscopic force (Figs. 4 (a) and 5
 452 (a)) and the correlation length (Fig. 5 (ac)). The influence of Young's modulus on the standard deviation amplitude of force
 453 fluctuations is more complex and displays a co-dependency with the cohesion values (Fig. 45 (b)). From For low to (respectively,
 454 high) cohesion values, the standard deviation evolves from amplitude of force fluctuations shows a decreasing to
 455 an (respectively, increasing) trend with Young's modulus, respectively. The influence of Young's modulus on the correlation
 456 length is weak (Fig. 4 (e)), as we observe mainly quasi-constant values over Young's modulus values. However, we notice a
 457 decreasing trend for large Young's modulus and low cohesion. Regarding the influence of the cohesion and friction angle, it
 458 is observed that increasing these parameters this parameter increases the three statistical indicators.

459 Finally, increasing the friction coefficient, generally also leads to an increase of the three statistical indicators. Note
 460 however that, over the range of explored friction coefficient values (0.2-0.5), the sensitivity to this parameter is less important
 461 than for the other two mechanical parameters (where E is varied over two orders of magnitude and C is varied over one order
 462 of magnitude). Despite changes in absolute force values, the evolution of the force profiles (Figs. S14, S18 and S22) and
 463 statistical indicators (Figs. S15, S19 and S23) with the mechanical parameters follow similar trends for all the samples, attesting
 464 to a moderate influence of the snow type. Nevertheless, it has to be noticed that the influence of Young's modulus on the
 465 correlation length is more pronounced for the RGl (Figs. S14, S15) and the DH (Figs. S18, S19) samples. We must highlight
 466 that due to large computing times, fewer parameter values have been explored for large Young's modulus. It is the case
 467 especially for the PP sample for which no numerical simulations for a Young's modulus of 1×10^{10} Pa has been performed as
 468 computing times were too long ($E = 1 \times 10^8$ Pa, $t \sim 4$ months and $E = 1 \times 10^9$ Pa, $t \sim 10$ months) to be achieved.

Formatted: Font: Italic

Formatted: Font: Italic

Formatted: Font: Italic

Formatted: Font: Italic

Formatted: Font: Italic

Formatted: Font: Italic

Formatted: Font: Italic

Formatted: Font: Italic

Formatted: Font: Italic

Formatted: Font colour: Auto

Formatted: Font colour: Auto

Formatted: Font colour: Auto

Formatted: Font colour: Auto

Formatted: Font colour: Auto

Formatted: Font colour: Auto

Formatted: Font colour: Auto

Formatted: Font colour: Auto

Formatted: Font colour: Auto

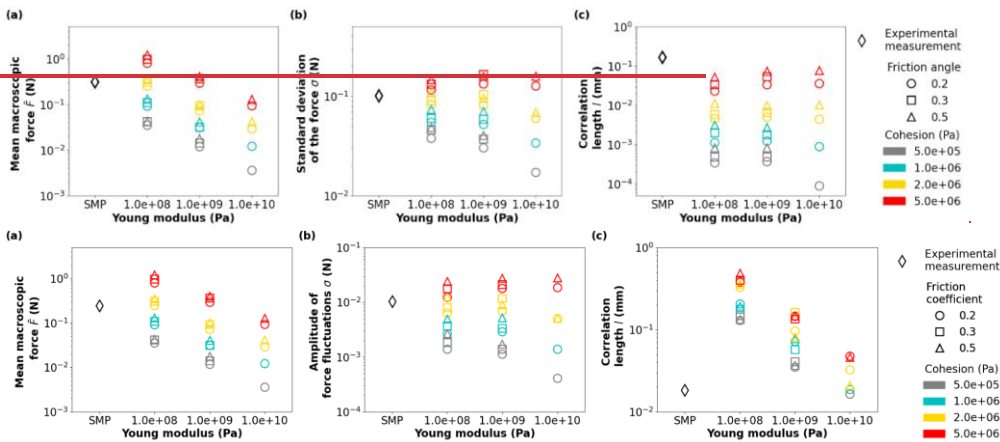


Figure 5: Evolution of statistical indicators as functions of Young's modulus, cohesion and friction angle coefficient: (a) Mean macroscopic force \bar{F} , (b) standard deviation amplitude of the force fluctuations σ , and (c) correlation length l . The experimental results (black diamonds) have been added to are also represented in the plots. Results The results presented here correspond to the RG sample.

The number of broken bonds with-per increment of tip penetration depth appears rather insensitive to Young's modulus (Figs. S12 (a), S16 (a), S20 (a), S24 (a)) and is only slightly reduced when cohesion increases (Figs. S12 (b), S16 (b), S20 (b), S24 (b)). Conversely, this quantity is significantly affected by the friction angle shows a pronounced influence coefficient, with an increase in-of the average bond failures failure rate when this parameter ($\tan(\phi)$) increases (Figs. S12 (c), S16 (c), S20 (c), S24 (c)).

Finally, it is observed that the influence of all the mechanical parameters on the radial grain displacement profiles is negligible (Figs. S13, S17, S21, S25). Young's modulus has shows no influence on the vertical grain displacement either. Cohesion only plays appears to play a role on the vertical displacement profile for the RGr sample, by enhancing upward movements. Larger friction angles coefficients tend to increase the downward movement of the grains close to the tip for all the snow types.

3.3 Comparison of DEM results with experimental measurements

The results of the DEM numerical model are compared to the experimental results to evaluate its predictive capability. First, it can be noted A first noticeable observation is that, for the values of the mechanical parameters tested, the orders of magnitude of the statistical indicators, obtained numerically and experimentally are similar for are consistent with the experimental results in most of the cases (Figs. 5, S15, S19, S23, Table S2), proving, Table S3). This demonstrates that the DEM model can reproduce is indeed capable of reproducing the main characteristics of the CPT force profile characteristics (Fig. S26, Table

Formatted: Font colour: Auto

Formatted: Font colour: Auto

Formatted: Font colour: Auto

Formatted: Font: Italic

Formatted: Font colour: Auto

Formatted: Font colour: Auto

S2). However, we highlight the difficulty to match of matching the three statistical indicators at once for a given combination of the three mechanical parameters studied. Hence, for the RG sample (Fig. 5), the DEM simulations fit well with simulation can reproduce the experimental mean macroscopic force and the standard deviation of the measured amplitude of force profiles, fluctuations but tends to underestimate/overestimate the correlation length, by a factor of 8 for the best combination of mechanical parameters. For the RGIr and DH samples (Figs. S15, S18), all the experimental statistical indicators can be reproduced individually, but not for one single combination of the mechanical parameters tested. For the PP sample, the experimental mean macroscopic force and the amplitude of force fluctuations can be well reproduced numerically, but the correlation length is underestimated (Fig. systematically overestimated by a factor of at least 8 (Fig. S23). The standard deviation can be approached for large Young's modulus and cohesion values. However the dataset is incomplete to provide a strong insight.

Sample	E (Pa)	C (Pa)	tan(ϕ)	Error $RE_{\bar{F}}$	Error σRE_{σ}	Error RE_{l_c}	Total error RE_{tot}
RG	1×10^9	5×10^6	0.2	-5.012×10^{-21}	31.2×10^{-1}	-8.952×10^{-1}	85.6×10^1
RGIr	1×10^{10}	21×10^6	0.23	-2.955×10^{-12}	5.546×10^{-1}	-1.21×10^{-1}	7.048×10^{-1}
DH	1×10^{10}	25×10^6	0.32	1.29×10^{-1}	3.311×10^{-1}	-6.723×10^{-1}	8.931×10^{-1}
PP	1×10^{10}	2×10^6	0.25	4.513×10^{-21}	3.916×10^{-1}	-9.965×10^{-1}	1.169×10^{-1}

Table 3: Selected combination of mechanical parameters for RG, RGIr, DH and PP samples. The indicated values of Young's modulus E , cohesion C and friction angle coefficient $\tan(\phi)$ correspond to the combination combinations that yields yield the lowest total error RE_{tot} on the statistical indicators (mean force \bar{F} , standard deviation macroscopic force σ , amplitude of force fluctuations σ , correlation length l) measured experimentally. Error values for all the mechanical parameters parameter combinations tested are indicated in Table S2S3.

Based on the sensitivity analysis (Sect. 3.2.3.), we selected for each sample the combination of the three mechanical parameters that minimises the total error for the different samples RE_{tot} (Tables 3, S2S3). The associated corresponding simulated force profiles produced by the DEM simulations (referred to as 'Numerical simulation 1') are compared with the experimental profiles in Fig. 6. From a qualitative point of view, a good match overall agreement is obtained observed between these numerical and experimental force profiles. For the RG sample, the experimental mean macroscopic force is well reproduced but the standard deviation is slightly overestimated by 20% by the numerical result, the amplitude of force fluctuation is overestimated by ~70% and the correlation length is slightly underestimated/largely overestimated by a factor of ~8 (Figs. 5, 6 (a), Table 3). Note that the mean force obtained numerically is underestimated in the first 3.5 mm of penetration compared to the experimental data. The experimental profile appears quasi linear in this upper section, and does not display the S-shape observed on the numerical profile (Sect. 3.1.) for the range of depth presented here. However, observing the force profile over a larger depth range allows us to observe this 'S' shape (Fig. S26). Both the experimental and numerical force profiles then reach a quasi-steady-state value at about the same depth (~6 mm, S27). For the RGIr sample, the correlation

length is well reproduced, while the mean force is slightly underestimated and the standard deviation is underestimated by a factor of ~ 0.5 (Figs. S15 and 6 (b), Table 3). It appeared difficult to reproduce experimental mean macroscopic force is fairly reproduced ($RE_F = 5\%$). The amplitude of force fluctuations is underestimated by $\sim 60\%$ and the correlation length is overestimated by $\sim 35\%$ (Figs. S15 and 6 (b), Table 3). We note that the slope change between 2.5 and 3 mm penetration depth is reproduced numerically. However, it appeared difficult to reproduce numerically the amplitude of force fluctuations in the upper section (from 0 to 4 mm) of the experimental profile. Both experimental and numerical profiles present a 'S' shape with a first slope change at around 3 mm of penetration. The simulations do not reproduce the force decrease after 6 mm observed in the experiments. For the DH sample, the experimental mean macroscopic force is well reproduced, overestimated by 25%. The standard deviation experimental amplitude of force fluctuations is slightly underestimated by 28%, and the correlation length is underestimated by more than 60% about half of the experimental value (Figs. S19, 6 (c), Table 3). The numerical results minimise the large force peaks observed in the upper part of the profile. Yet, it appears that the simulations fairly reproduce the general shape of the experimental profile (above 3 mm) but reproduce fairly well the main features of the amplitude of force fluctuations, especially the force "jump" at 3 mm depth. Finally, for the PP sample, the experimental mean macroscopic force is well reproduced, while the standard deviation (underestimated by $\sim 30\%$, while the experimental amplitude of force fluctuations is underestimated by 60%) and%. In this case, the experimental correlation length (1 order of magnitude) are underestimated could not be reproduced at all, with values overestimated by a factor of at least 80 (Figs. S23 and 6 (d), Table 3).

Formatted: Font colour: Auto

Formatted: Font colour: Auto

Formatted: Font colour: Auto

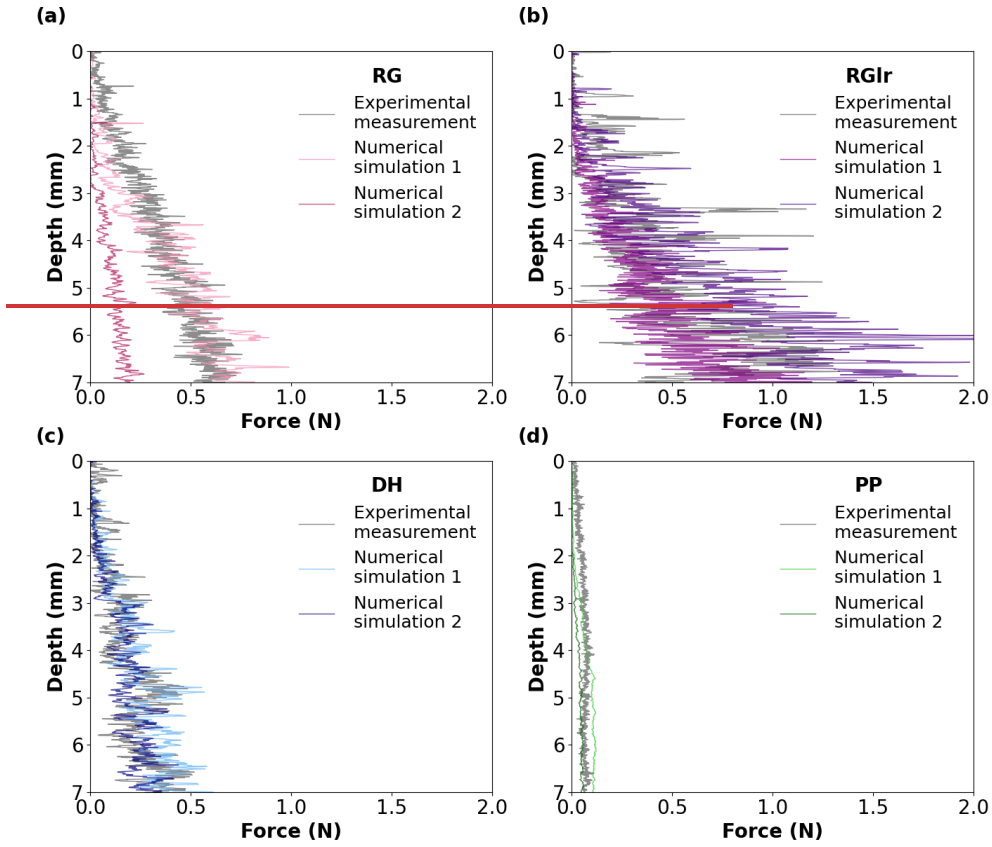
Formatted: Font colour: Auto

Formatted: Font colour: Auto

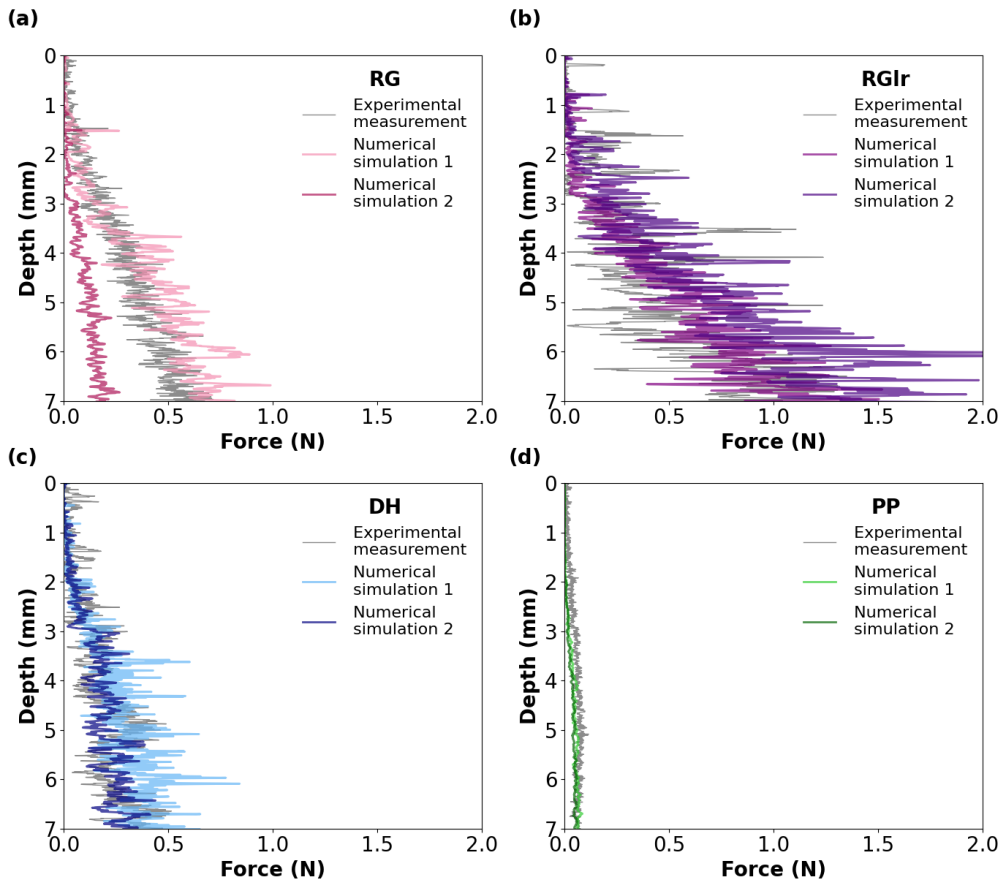
Formatted: Font colour: Auto

Formatted: Font colour: Auto

Formatted: Font colour: Auto



540



541
 542 Figure 6: Experimental (grey) and numerical (coloured) CPT force profiles obtained for (a) RG, (b) RGlR, (c) DH, and (d) PP
 543 samples. The “Numerical simulation 1” profiles correspond to the best fit of the mechanical parameters determined for each sample
 544 (Table 3), while “Numerical simulation 2” profiles correspond to the overall best fit of the mechanical parameters for the four
 545 samples RG, RGlR, DH and PP ($E = 1 \times 10^9$ Pa, $C = 2 \times 10^6$ Pa and $\tan(\varphi) = 0.2$, Table S2S3).

546
 547 In addition For comparison, we also selected the single set of mechanical parameters that minimises the combined total error
 548 RE_{tot} on RG, RGlR, DH and PP samples. Corresponding values are: $E = 1 \times 10^9$ Pa, $C = 2 \times 10^6$ Pa and $\tan(\varphi) = 0.2$. The
 549 respective errors for each sample can be found in Table S2S3. In general, the associated corresponding simulated force profiles
 550 computed numerically agree fairly well with the experimental results (referred to as ‘Numerical simulation 2’ in Fig. 6)-6)

Formatted: Font: Italic

Formatted: Font: Italic

Formatted: Font: Italic

Formatted: Font: Italic

Formatted: Font: Italic

Formatted: Font: Italic

Formatted: Font: Italic

Formatted: Font colour: Auto

Formatted: Font colour: Auto

551 also show a fair agreement with the experimental results. For the RG sample, however, the standard deviation is well
 552 reproduced, while the experimental mean macroscopic force and correlation length are significantly underestimated by 70%
 553 (Figs. 4, 5, 6 (a), Table S2). For RGIr, the agreement is good. The numerical amplitude of force fluctuations reproduces the
 554 experimental value at ~70%, while the correlation length is significantly overestimated by a factor of 5. For the RGIr sample,
 555 the agreement is acceptable for the three statistical indicators (relative errors between 3915% and 4740%). For the DH sample,
 556 the experimental mean macroscopic force is well-reproduced, at 90%, while the standard deviation experimental amplitude of
 557 force fluctuations is slightly underestimated (factor of 0.4) by 60% and the experimental correlation length is underestimated
 558 (by about 80%) overestimated by a factor ~2. Finally, for the PP sample, the experimental mean macroscopic force and
 559 underestimated by ~80%, the standard deviation are underestimated by about 50% amplitude of force fluctuations by 85% and
 560 the experimental correlation length is underestimated by about 100% again strongly overestimated by a factor of 20 (Figs. S23
 561 and 6 (d), Table 3).

Formatted: Font colour: Auto

Formatted: Font colour: Auto

Formatted: Font colour: Auto

Formatted: Font colour: Auto

Formatted: Font colour: Auto

Formatted: Font colour: Auto

Formatted: Font colour: Auto

Formatted: Font colour: Auto

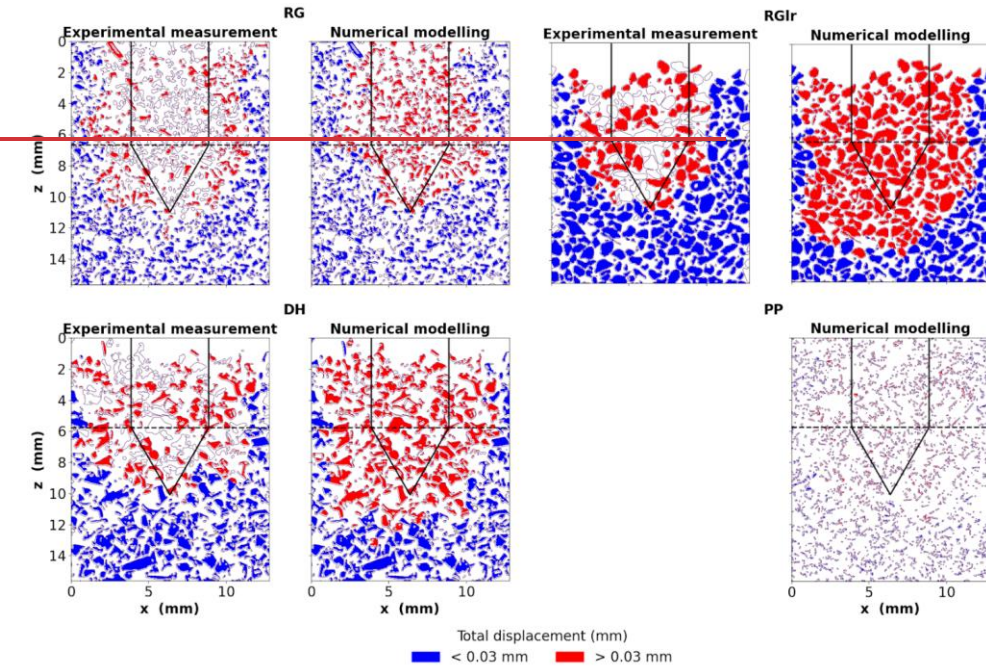
Formatted: Font colour: Auto

Formatted: Font colour: Auto

Formatted: Font colour: Auto

Formatted: Font colour: Auto

Formatted: Font colour: Auto



Formatted: Font colour: Auto

Formatted: Font colour: Auto

Formatted: Font colour: Auto

Formatted: Font colour: Auto

Formatted: Font colour: Auto

Formatted: Font colour: Auto

Formatted: Font colour: Auto

Formatted: Font colour: Auto

Formatted: Font colour: Auto

Formatted: Font colour: Auto

Formatted: Font colour: Auto

Formatted: Font colour: Auto

Formatted: Font colour: Auto

Formatted: Font colour: Auto

Formatted: Font colour: Auto

Formatted: Font colour: Auto

Formatted: Font colour: Auto

Formatted: Font colour: Auto

Formatted: Font colour: Auto

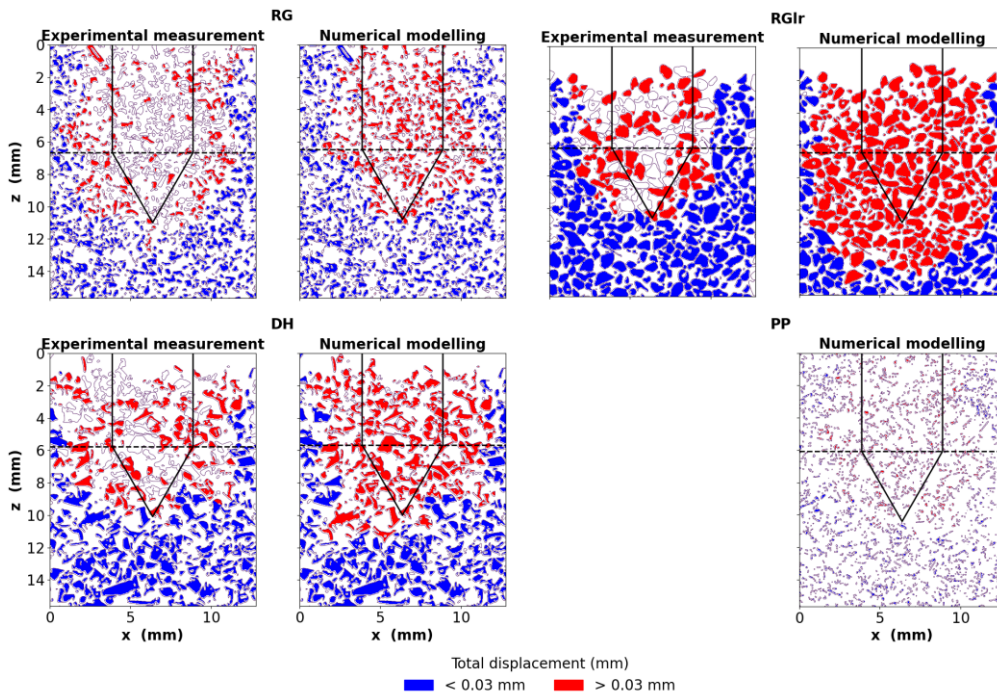
Formatted: Font colour: Auto

Formatted: Font colour: Auto

Formatted: Font colour: Auto

Formatted: Font colour: Auto

563



564
 565 Figure 7: Total displacement maps obtained experimentally with μ CT (left panels) and numerically with DEM simulation
 566 (right panels) for the RG, RGr, DH and PP samples. A displacement threshold of 0.03 mm has been set to define the
 567 deformation zone (Peinke et al., 2020). White grains correspond to non-trackable grains in μ CT scans (Peinke et al., 2020) and
 568 deleted grains not represented in the DEM simulations. The final tip position is indicated with black solid lines. The horizontal black
 569 dashed line indicates the cone top. Displacement profiles shown in Fig. 8 are computed from the sample surface to the cone top.
 570 Numerical results are obtained with the combination of mechanical parameters indicated in Table 3. No experimental map is
 571 presented displacement field could not be determined for the PP sample due to the difficulties to apply the grain tracking algorithm
 572 for this sample.

573
 574 Qualitatively As shown in Fig. 7, the numerical and DEM simulations also proved capable of reproducing, at least qualitatively,
 575 the experimental grain displacement fields present similar patterns derived from μ CT scans for all the four snow types and
 576 both. Essentially similar results are obtained with the individual best-matching sets of selected mechanical parameters
 577 (Figs. indicated in Table 3 (Fig. 7), and S27 with the globally-matching set of parameters introduced in the previous paragraph
 578 (Fig. S28)). For the RG sample, the overall shape and size of the deformation zone is well reproduced by the simulations.
 579 The largest discrepancies are observed for the RGr sample, for which the radial and vertical extension and distribution of the
 580 deformation zone differ from the data derived from μ CT scans. The radial displacement obtained numerically displays a more

Formatted: Font colour: Auto

Formatted: Font colour: Auto

Formatted: Font colour: Auto

Formatted: Font colour: Auto

Formatted: Font colour: Auto

Formatted: Font colour: Auto

Formatted: Font colour: Auto

Formatted: Font colour: Auto

Formatted: Font colour: Auto

Formatted: Font colour: Auto

Formatted: Font colour: Auto

Formatted: Font colour: Auto

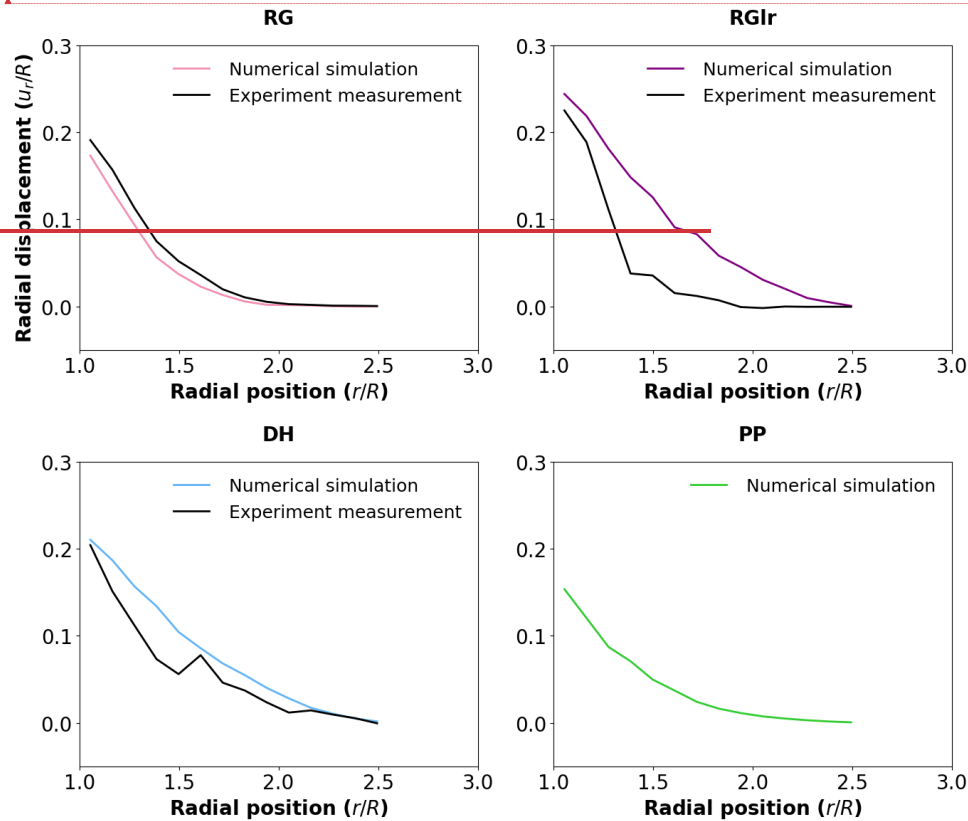
581 linear trend compared to the arcuate shape of the experimental radial displacement profile (Fig. 8). For the DH sample, the
 582 radial extension of the deformation zone is well reproduced by the simulations, but the vertical extension tends to be
 583 overestimated. Finally, the numerical results obtained for the PP sample could not be compared to experimental measurements
 584 as the grain tracking algorithm is not applicable on these small grains (Peinke et al., 2020). The numerical results attest of the
 585 accordance of the deformation zone with other numerical profiles obtained for other snow types. The largest discrepancies are
 586 observed for the RGIr sample, for which the radial and vertical extensions of the deformation zone are overestimated compared
 587 to the experimental data.

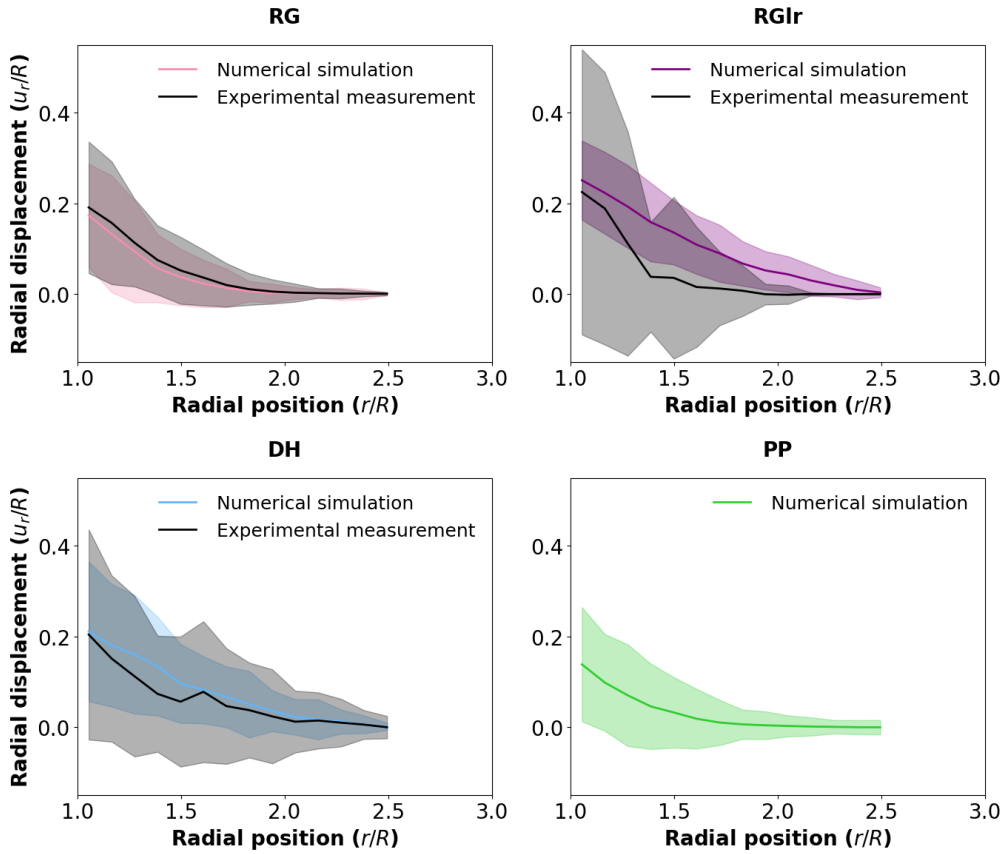
Formatted: Font colour: Auto

Formatted: Font: Arial, 12 pt

Formatted: Font: Arial, 12 pt, Font colour: Auto

Formatted: Border: Top: (No border), Bottom: (No border), Left: (No border), Right: (No border), Between : (No border)





590 **Figure 8: Radial displacement profiles (solid lines) obtained experimentally (black) and numerically (coloured) for the RG, RGIr,**
 591 **DH and PP. Numerical samples. The shadowed areas around the solid lines correspond to the standard deviation of grain**
 592 **displacement and exhibit the variability of the radial displacement of grains. The numerical results are obtained with the**
 593 **combination of mechanical parameters indicated in Table 3.**
 594

595
 596 Radial Similarly, the radial displacement profiles obtained withfrom the DEM numerical modelsimulations are overall in good
 597 agreement with their experimental counterparts (FigFigs. 8 and S29). Consistently with the displacement maps, the largest
 598 discrepancy is observed for the RGIr sample. In particular, the abrupt slope break seen in the experimental profile at a radial
 599 position of about 1.5 is not reproduced in the numerical profile. Note however that, due to a relatively low number of trackable
 600 grains (Fig. 7), the standard deviation of the grain radial displacements is larger in the experimental measurements, which may

601 result in a larger uncertainty on the average profile. In contrast, simulations on the RG and DH samples show a very good
602 agreement with the experiments. The ΔZ (CZ (defined with displacement threshold set at 0.03 mm) obtained from numerical
603 simulations extend radially up to 1.7R, 2.2R, 2.2R and 1.8R for the RG, RGl, DH and PP samples,
604 respectively. In comparison, the CZ derived from CT scans extend up to 1.8R,
605 1.7R and 2.2R for the RG, RGl and DH samples, respectively (no measurement for PP sample).

606 4 Discussion

607 4.1 Evaluation of the DEM model

608 We used three mechanical parameters, namely Young's modulus, the cohesion and the friction coefficient, to adjust the
609 simulated force profiles to the experimental results. Overall, the numerical model could satisfactorily reproduce relatively
610 well the mechanical response of all studied numerical samples with a single set of mechanical parameters ($E = 1 \times 10^9$ Pa, C
611 $= 2 \times 10^6$ Pa and $\tan(\phi) = 0.2$) (Fig. 6), indicating that the characteristics of differences in the force profiles among the samples
612 are mainly dependent of the snow microstructure.

613 It should also be noted that the values of the mechanical parameters obtained by adjusting the model on the experimental data
614 (either globally for all samples, or for each sample individually, Table 3) are reasonably close to the mechanical properties of
615 ice. Young's modulus of ice is measured between 9×10^9 Pa and 10×10^9 Pa (Gammon et al., 1983), while our selected values
616 range between 1×10^9 Pa and 1×10^{10} Pa (except for PP sample). In practice, recall that, in YADEF, the numerical Young's
617 modulus is a numerical parameter used in YADEF software to parameterize the normal contact stiffness, and is not
618 directly expected to necessarily correspond to the physical Young's modulus of the material. In particular, the numerical
619 Young's modulus may depend on the grain shape representation and/or the choice of the contact law. (Sect. 2.2.2).
620 Nevertheless, the fact that the numerical value of E is close to that in the same range of magnitude as the elastic properties of
621 ice provides good confidence that the DEM model and the used contact law (Eq. (1), Eq. (2), Eq. (3))-(5)) correctly
622 capture the physical processes at play. Similarly, the numerical cohesion values, ranging between 2×10^6 Pa and 5×10^6 Pa,
623 are in agreement with typical cohesion values measured on ice (in the range 2×10^6 Pa to 6×10^6 Pa, Schulson and Duval,
624 2009). Finally, numerical friction coefficients appear to be on the order of 0.2–0.35, while values measured
625 experimentally are generally ranging from 0.02 to 1 (Fish and Zaretsky, 1997; Maneno and Arakawa, 2004). All these
626 results reinforce the confidence in the relevance of the DEM model credibility.

627 We acknowledge that the mechanical parameters obtained from minimising the errors on the statistical indicators do not
628 necessarily represent optimal values, in the sense that only a limited number of parameter sets could be tested. In particular,
629 due to a high computational cost, few simulations performed with $E = 1 \times 10^{10}$ Pa were achieved for RG, RGl and DH
630 samples. Based on the sensitivity analysis, a more proper inversion procedure could be developed to retrieve true optimal
631 values of the mechanical parameters. This would certainly provide more robust elements as to determine whether a single set
632 of mechanical parameters can be used to represent the experimental results of all snow types, or whether these mechanical

Formatted: Font colour: Auto

Formatted: Font: Italic

Formatted: Font colour: Auto

Formatted: Font colour: Auto

Formatted: Font colour: Auto

Formatted: Font: Italic

Formatted: Font: Italic

Formatted: Font: Italic

Formatted: Font colour: Auto

Formatted: Font colour: Auto

Formatted: Font: Italic

633 parameters differ according to the snow ~~types. In our type. Our~~ current analysis, ~~the cannot provide a conclusive~~ answer to this
634 question ~~remains ambiguous.~~ Note that ice is a polycrystalline material, whose mechanical behaviour can be strongly
635 anisotropic depending on the ice structure (Fish and Zaretsky 1997; Thorsteisson, 2001; e.g. Maeno and Arakawa, 2004).
636 ~~Therefore, it is thus~~ not unlikely that ice bonds between grains ~~can~~ be characterised by different mechanical properties
637 depending on the specific conditions of snow formation and evolution.

638 As further proof of ~~DEM's good~~ DEM predictive capabilities, we could ~~also~~ observe that the grain displacement fields measured
639 for the different snow types were overall well reproduced by the simulations (Figs. 7 and 8). In particular, the model captures
640 the radial extent of the deformation zone, ~~i.e. of which is on~~ the order of ~~1.5R-2-2.5R, 2R~~. A discrepancy between the numerical
641 and experimental ~~profiles of~~ radial displacement ~~profiles~~ was observed for the RGlR sample. ~~It should, however, However, it~~
642 ~~can~~ be noted that these experimental radial displacement profiles for the RGlR sample ~~are also these with~~ show the largest
643 divergence ~~compared to with~~ the prediction of the cavity expansion model (CEM) (Yu and Carter, 2002), as shown by Peinke
644 et al. (2020). In fact, the radial profile predicted by the CEM ~~for this sample~~ is similar to the radial profile obtained numerically
645 in this study.

646 4.2 Interpretation

647 4.2.1 ~~Mechanical Sensitivity to the mechanical~~ parameters ~~sensitivity~~

648 The sensitivity analysis revealed a strong influence of the mechanical parameters on the simulation results. In particular, a
649 clear dependence of the mean macroscopic force with Young's modulus E was observed, suggesting that a significant part of
650 the sample undergoes elastic deformation, while brittle failures are confined in a region close to the tip. Note that a similar
651 dependence to E with a cohesive contact law has been observed in DEM modelling of soil compression (De Pue et al., 2019)
652 and snow compression (Bobillier et al., 2020). ~~The larger mean macroscopic force, the amplitude of force fluctuations and the~~
653 ~~correlation length all increase with the~~ cohesion C and, to a smaller extent, ~~with the~~ friction ~~angle, also tend to increase the~~
654 ~~mean force, the standard deviation and the correlation length-coefficient $\tan(\phi)$.~~ This can be related to the fact that increasing
655 cohesion and friction between grains increase bond strength. It ~~is was~~ also observed that cohesion tends to prevent bond failures,
656 and to favour the upward movement of grains for samples with ~~the largest a large~~ initial density, such as RGlR. In contrast,
657 increasing the friction ~~angle coefficient~~ enhances the bond failure rate and the downward movement of grains (Figs. S12, S16,
658 S20, S24). When sliding between grains is inhibited, a grain dragged by the tip movement will ~~drag down~~ entrain surrounding
659 grains more easily, thus enlarging the deformation zone and triggering additional bond failures. Finally, radial grain
660 displacements and the radius of the deformation zone ~~are appeared to be~~ mostly insensitive to the mechanical parameters,
661 indicating that ~~these features are mainly controlled by~~ CPT configuration and snow ~~type mainly control these~~
662 ~~features~~ microstructure.

Formatted: Font: Italic

Formatted: Font: Italic

663 4.2.2 Compaction zone development

664 For all snow types, the force profiles computed numerically display a ‘S’ shape (Figs. 1, S6, S8, S10). We attribute this shape
665 to the development of a compaction zone (CZ) in front of the tip during its progressive penetration into the numerical sample.
666 More specifically, the first stage of the force profiles (slope increase) might be presumably caused by the progressive entry
667 of the cone penetration, before the cylindrical part reaches into the sample. The second stage (constant slope) is attributed to
668 the development of the CZ in front of the tip. The third stage (quasi-constant force value) suggests that a steady-state regime,
669 with a fully-developed CZ, is reached. Depending on the snow type, the numerical results suggest indicate that full development
670 of the CZ occurs for 5.56 mm to 8 mm of penetration depth. These results agree with the experimental profiles for the RG, DH
671 and PP samples. For the RGI sample, the experimental penetration profile did not reach the steady-state stage. Globally, we
672 can highlight that the DEM simulations are able to reproduce fairly well the global shape of the experimental profiles, and thus
673 to correctly capture the development of the CZ.

674 Nevertheless, in another experimental study, the CZ has been reported to be fully developed only for around 40 mm of depth
675 penetration (Herwijnen, 2013), which is significantly deeper than the experimental and numerical results obtained in this study.
676 A first hypothesis to explain this observation discrepancy is that if since the maximum depth of our CPT force profiles reach a
677 maximum depth of is 10 mm, we might thus miss information on the full CZ development. A second hypothesis explanation
678 could be related to the differences in the experimental set-up setups. Indeed, Peinke et al. (2020) performed CPT on snow
679 samples contained in cylinders of 20 mm diameter and 20 mm height, which is significantly smaller than the
680 decimetric snow samples considered by Herwijnen (2013). Boundary effects might thus play a role in limiting the development
681 of the CZ. Finally, the tip geometry also differs between the two studies. Peinke et al. (2020) used a plain tip, while Herwijnen
682 (2013) used the original SMP tip geometry with a cone radius larger than the rod. A sensitivity analysis comparing the two
683 geometries showed an influence over the upper 12 mm of the force profiles (Peinke, 2020). The plain tip geometry
684 produced resulted in larger values of the mean macroscopic force and standard deviation the amplitude of force fluctuations
685 values. This sensitivity effect might also influence the characteristics of the CZ development, which could be studied in the
686 future using the presented numerical model.

687 4.2.3 Grain-tip interaction

688 The sensitivity analysis to the grain shape representation (Sect. S1.1) provides interesting insights into the interpretation of
689 force profiles. In particular, the study highlighted that the grain shape representation could be relatively coarse (high volumetric
690 error E_V) but still produce a force profile with an acceptable mechanical error E_M compared to a reference profile obtained for
691 a fine grain shape representation ($E_V < 10\%$) (Fig. S1, Table S1). This is notably the case for the RG sample, as for which the
692 selected grain shape representation ($R_L = 5$, $S = 0.3$) corresponds to a value of E_V of about 40%. Larger values of E_V
693 often imply grain loss, as the smallest grains identified in the μ CT scans cannot be represented by the DEM in this case. Despite
694 this loss with coarse spherical elements. Yet, the similarity of the force profile to the reference force profile indicates the limited

Formatted: Font colour: Auto

Formatted: Font colour: Auto

Formatted: Font colour: Auto

Formatted: Font: Italic

Formatted: Font: Italic

Formatted: Font: Italic

Formatted: Font: Italic

Formatted: Font: Italic

Formatted: Font: Italic

695 contribution of these smallest grains to the macroscopic force, compared to the largest grains with stronger bonds. The loss of
 696 grains and bonds might nevertheless directly affect the force fluctuations, providing a potential explanation for why the
 697 DEM model underestimates the correlation length obtained experimentally for the samples with the smallest grain sizes (RG
 698 and PP) (Figs. 5, S23).

699 **4.2.3 Scaling relation for the mean macroscopic force**

700 To try and synthesise the large number of simulation results obtained in this study, scaling relations describing the evolution
 701 of the statistical indicators as a function of the main simulation parameters can be looked for. We focused in particular on the
 702 mean macroscopic force \bar{F} , which was observed to depend both on the mechanical parameters E , C and $\tan(\varphi)$, as well as on
 703 sample microstructure. Since the range of friction coefficient values (between 0.2-0.5) that we could explore remained limited
 704 compared to the ranges of E and C , the parameter $\tan(\varphi)$ was not included in this analysis and the results presented below
 705 correspond to a single value $\tan(\varphi) = 0.3$.

706 First, inspection of our results (see Figs. 5 (a), S15 (a), S19 (a), S23 (a)) indicates that the dependencies of the mean
 707 macroscopic force \bar{F} to the Young's modulus E and cohesion C appear to be consistent across the four tested samples (see also
 708 Table S4). More precisely, \bar{F} scales with E according to a power law of the form $\bar{F} \sim C^{-\alpha}$, with an exponent α on the order of
 709 $1/2$. Similarly, \bar{F} scales with C according to a power law of the form $\bar{F} \sim C^{\beta}$, with β on the order of $3/2$.

710 Second, we can expect \bar{F} to be also related to the rate of cohesive broken bonds per unit penetration depth. In particular, it is
 711 observed (see Figs. S12, S16, S20, S24) that the slope λ of the cumulative proportion of broken bonds as a function of depth
 712 is essentially independent of the Young's modulus and cohesion. Conversely, as shown in Fig. 9 (a), this slope λ is linearly
 713 related to the initial contact density ν defined as:

$$714 \nu = z\Phi \quad (10)$$

715 with z the coordination number (number of initial cohesive interactions between grains divided by the number of grains, see
 716 Table 1) and Φ the volume fraction of the sample (ice density = 917 kg m^{-3} , see Table 1).

718 From these different observations, the following scaling law for the mean macroscopic force \bar{F} can be proposed:

$$719 \bar{F} = B T C \left(\frac{C}{E}\right)^{\alpha} f(\nu) \quad (11)$$

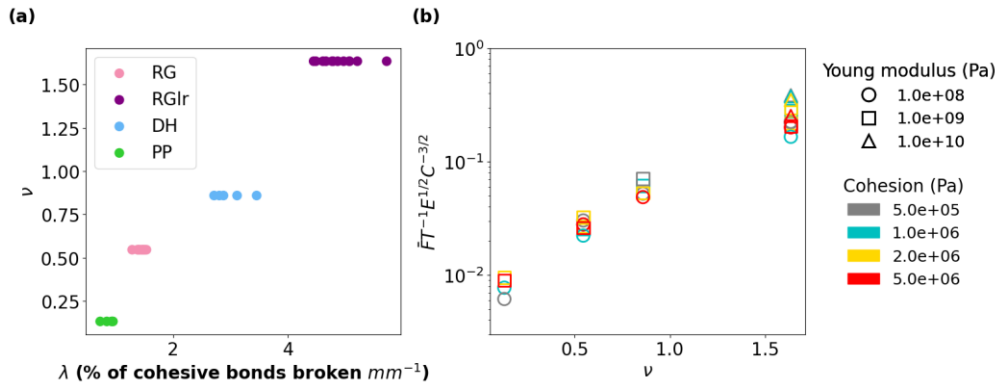
720 with B a dimensionless constant, T (m^2) the surface area of the cone (with a radius R and a cone apex a , Table 2) in contact
 721 with the sample, and f a function to be determined. Figure 9 (b) shows the dimensionless quantity $\bar{F} T^{-1} E^{1/2} C^{-3/2}$ plotted against
 722 the initial contact density ν . We observe that all the simulation results for the four snow types and the different values of
 723 Young's modulus and cohesion nicely merge on a unique logarithmic trend. Note, however, that a relatively larger dispersion
 724 is observed for RGlR ($\nu = 1.63$) compared to the other samples.

725 **Equation (11) encapsulates in a single relation the main physics controlling the mean macroscopic force recorded by**
 726 **the penetrometer. In particular, this relation indicates that the influence of snow microstructure can be captured, at**

727 least as a first approximation, by the initial contact density ν . Former studies already showed that this parameter plays
728 a key role in the mechanical behaviour of cohesive granular materials (Gaume et al. 2017). 4.2.4 Cohesive bond failure

Formatted: Font colour: Auto

729 In our DEM simulations, once broken, the cohesive interactions between grains disappear. New interaction between grains
730 will be frictional only. Hence, we assume that bonds between grains in contact cannot reform at the time scale of the
731 experiments. Indeed, the measurements last less than 1 s (tip velocity = 20 mm s⁻¹ and sample holder height = 20 mm), while
732 the mechanisms involved in the sintering process are generally slower (Blackford, 2007). However, subsecond sintering
733 (millisecond process) caused by the freezing of a thin quasi-liquid layer between two grains in contact has been observed, even
734 at low temperature (Szabo and Schneebeli, 2017). Looking for similar relations describing the other statistical indicators (amplitude
735 of force fluctuations and correlation length) constitutes an interesting prospect for future analyses, although we can anticipate
736 these indicators to display more complex dependencies. Further analyses will also be required to explore the influence of the
737 friction coefficient on these relations.



739 **Figure 9: (a) Initial contact density ν versus the slope λ of the proportion of cohesive bonds broken per unit depth (mm⁻¹) for each**
740 **snow type. The values of initial contact density ν were computed with Eq. (10) and the values indicated in Table 1. The slopes λ were**
741 **computed from the evolution of the cumulative proportion of cohesive bonds broken (Figs. S12, S16, S20, S24) over a window of 7**
742 **mm depth. (b) Dimensionless quantity $FT^{-1}E^{1/2}C^{-3/2}$ (see Eq. (11)) versus the initial contact density ν for all simulation results. All the**
743 **results are provided for a friction coefficient $\tan(\phi)$ of 0.3.**

745 ~~2007). Including this subsecond sintering in the numerical simulations shall be considered in future works to study its~~
746 ~~role on the mechanical response of the samples.~~

Formatted: Heading 1

747 5 Conclusion

748 We have evaluated a numerical model based on DEM that reproduces the mechanical behaviour of snow in the brittle regime.
749 The DEM model ~~is taking~~takes into account the ice properties and the snow microstructure captured by tomography. The

750 experimental configuration of the CPT measurements conducted on different snow types by Peinke et al. (2020) has been
751 reproduced with the DEM model. Three parameters namely, the mean ~~macroscopic~~ force, the ~~standard deviation~~ amplitude of
752 ~~the force fluctuations~~ and the correlation length, were used to quantify the similitude of the numerical and experimental
753 profiles. The grains displacement field was computed and compared to the experimental displacement field derived from μ CT
754 scans acquired before and after the CPT.

755 The DEM model has demonstrated overall a good capability to ~~simulate~~ reproduce the mechanical responses of CPT performed
756 in different snow types. The computed force profiles satisfactorily reproduce the main characteristics of the experimental force
757 profiles. The results revealed that the force ~~profiles~~ profile characteristics are ~~mainly~~ strongly dependent on the microstructure.
758 A sensitivity analysis ~~proved also demonstrated~~ the dependence of the mechanical response to the mechanical parameters of
759 the contact law. In particular, a simple scaling law could be derived relating the mean macroscopic force computed by the
760 DEM to the mechanical parameters E (Young's modulus) and C (cohesion) and to the microstructure characteristics captured
761 by the initial contact density. The displacement fields are also well reproduced by the model, except for the RGl_r sample
762 showing a larger extent for the numerical results. The agreement in terms of radial displacement profiles is very good. The
763 grains are mainly travelling downward during the CPT, although for the RGl_r sample, the upward ~~movement of the~~
764 ~~grains movements~~ close to the surface ~~is~~ are not negligible. The CPT implies a complex deformation field with a compression
765 zone around the apex and an expansion zone close to the surface (Peinke et al., 2020). Therefore being able to reproduce the
766 force profiles (including high-frequency fluctuations) and displacement ~~profiles~~ fields for this mechanical test
767 ~~constitute~~ constitutes a strong validation of the reliability of the DEM model.

768 ~~The CPT modelling via DEM model brings advantages to reproduce and interpret the snow mechanical behaviour to CPT~~
769 ~~compared to others interpretation models as it is able to take into account the high frequency fluctuations and predict the~~
770 ~~displacement field and.~~ However, a major downside of the DEM method is their high computational cost, (simulation times
771 ranging between 1 week to several months according to depending on the physical and numerical parameters for the chosen
772 CPT configuration, ~~preventing us from exploring all~~, which limited the range of mechanical parameters ~~chosen~~ that could be
773 explored for all ~~the~~ snow types. ~~Besides, the DEM model could be improved by adding time dependent parameters in the~~
774 ~~contact laws to take into account the sintering process.~~

775 The developed DEM model nonetheless constitutes a versatile approach that ~~can~~ could be applied to various materials and
776 configurations. in future studies. In particular, it will be possible to use the DEM model ~~can be used to study to gain more~~
777 physical insights into the interaction between the tip and the grains ~~of the numerical sample~~, in order to better interpret the
778 CPT force profiles. Pertinent Such analyses will provide ways to test and derive relevant macro- and micromechanical
779 parameters ~~could be derived~~ to characterise the microstructure properties from the CPT force signal solely. Especially In
780 particular, the validity of the assumptions made by the HPP-NHPP method, as well as the influence of the CZ development
781 ~~will be tested. Critical structural parameters driving the mechanical behaviour, could be identified and a parameterization~~
782 ~~developed in order to include the effect of snow microstructure in macroscale numerical models studying snowpack and~~

Formatted: Font colour: Auto

Formatted: Font colour: Auto

Formatted: Font colour: Auto

Formatted: Font colour: Auto

783 avalanches, will be assessed. Future studies may also consider refining the used contact laws to investigate, e.g. the influence
784 of sintering processes on CPT results.

785 **Code availability**

786 Codes can be provided by the corresponding [authors/author](#) upon request.

787 **Data availability**

788 All data can be provided by the corresponding [authors/author](#) upon request.

789 **Author contribution**

790 CH, PH and GC developed the numerical model, CH performed simulations and evaluated the numerical model, IP, PH, GC,
791 JR designed experiment, IP acquired experimental data, IP processed and analysed experimentation measurements, CH
792 analysed and interpreted numerical results, CH wrote the manuscript draft, PH and GC reviewed and edited the manuscript.

793 **Competing interests**

794 GC is a member of the editorial board of The Cryosphere. The peer-review process was guided by an independent editor, and
795 the authors have ~~also~~ no other competing interests to declare.

796 **Acknowledgements**

797 This work benefited from financial supports from the Centre National de la Recherche Scientifique (CNRS), the Centre
798 National de la Recherche Météorologique, the Agence Nationale de la Recherche (Project ANR MiMESis-3D ANR-19-CE01-
799 0009). We thank the two reviewers, Richard Parson and Henning Löwe, for their constructive feedback that enabled us to
800 significantly improve the quality of our manuscript.

801 **References**

802 Bartelt, P., and M. Lehning.: A physical SNOWPACK model for the Swiss avalanche warning: Part I—Numerical model,
803 Cold Reg. Sci.Technol.,35(3), 123–145, doi: 10.1016/S0165-232X(02)00074-5, 2002.
804 Bishop, R. F., Hill, R., and F Mott, N.: The theory of indentation hardness tests, Proc. Phys. Soc. 57:321, doi: 10.1088/0959-
805 5309/57/3/301, 1945.

Formatted: French (France)

806 ~~Blackford, J. R.: Sintering and microstructure of ice: a review, *J. Phys. D: Appl. Phys.* 40, R355–R385, doi: 10.1088/0022-~~
807 ~~3727/40/21/R02, 2007.~~

808 Bobillier, G., Bergfeld, B., Capelli, A., Dual, J., Gaume, J., Herwijnen, A., and Schweizer, J.: Micromechanical modeling of
809 snow failure, *The Cryosphere*, 14, 39–49, doi:10.5194/tc-14-39-2020, 2020.

810 Bobillier, G., Bergfeld, B., Dual, J., Gaume, J., Herwijnen, A., and Schweizer, J.: Micro-mechanical insights into the dynamics
811 of crack propagation in snow fracture experiments, *Sci Rep* 11, 11711, doi :10.1038/s41598-021-90910-3, 2021.

812 Bolton, M. D., Gui, M. W., and Phillips, R.: “Review of miniature soil probes for model tests,” in *Proceedings of the 11th*
813 *Southeast Asian Geotechnical Conference (Singapore)*, 85–90, 1993.

814 Brun, E., David, P., Sudul, M., and Brunot, G.: A numerical model to simulate snow-cover stratigraphy for operational
815 avalanche forecasting, *J. Glaciol.*, 38(128), 13–22, doi: 10.3189/S0022143000009552, 1992.

816 Calonne, N., F. Flin, C. Geindreau, B. Lesaffre and S. Rolland du Roscoat: Study of a temperature gradient metamorphism of
817 snow from 3-D images: time evolution of microstructures, physical properties and their associated anisotropy, *The Cryosphere*,
818 8, 2255-2274, doi: 10.5194/tc-8-2255-2014, 2014.

819 Calonne, N., F. Flin, B. Lesaffre, A. Dufour, J. Roulle, P. Puglièse, A. Philip, F. Lahoucine, C. Geindreau, J.-M. Panel, S.
820 Rolland du Roscoat and P. Charrier, CellDyM : a room temperature operating cryogenic cell for the dynamic monitoring of
821 snow metamorphism by time-lapse X-ray microtomography, *Geophys. Res. Lett.*, 42, doi: 10.1002/2015GL06354, 2015.

822 Coléou, C., B. Lesaffre, J.-B. Brzoska, W. Ludwig and E. Boller: Three dimensional snow images by X-ray microtomography,
823 *Ann. Glaciol.*, 32, 75-81, doi : 10.3189/172756401781819418, 2001.

824 Coeurjolly, D. and Montanvert, A. and Chassery, J.-M.: Descripteurs de forme et moments géométriques. *Géométrie discrète*
825 *et images numériques*, Hermès, 2007.

826 De Pue, J., Di Emidio, G., Verastegui Flores, R. D., Bezuijen, A., and Cornelis, W. M.: Calibration of DEM material parameters
827 to stimulate stress-strain behaviour of unsaturated soils during uniaxial compression, *Soil and Tillage Research*, 194, 104303,
828 doi: 10.1016/j.still.2019.104303, 2019.

829 Dowd, T. and Brown, R.L.: A new instrument for determining strength profiles in snow cover, *Journal of Glaciology*, 32(111):
830 299–301, doi: 10.3189/S0022143000015628, 1986.

831 Fierz, C., Armstrong, R. L., Durand, Y., Etchevers, P., Greene, E., and McClung, D. M.: “The international classification for
832 seasonal snow on the ground,” in *Tech. Doc. Hydrol. 83 Paris: UNESCO*, 2009.

833 Fish, A. M. and Zaretsky, Y. K.: Ice strength as a function of hydrostatic pressure and temperature, *CRREL report*, 38207814,
834 1997.

835 Floyer, J.A., and Jamieson, J.B. Rate-effect experiments on round-tipped penetrometer insertion into uniform snow, *Journal*
836 *of Glaciology*, 56(198): 664–672. doi:10.3189/002214310793146322, 2010.

837 Freitag, J., Wilhelms, F. and Kipfstuhl, S.: Microstructure dependent densification of polar firn derived from X-ray
838 microtomography, *J. Glaciol.*, 50(169), 243–250, doi: 10.3189/172756504781830123, 2004.

Formatted: French (France)

Formatted: French (France)

Field Code Changed

Formatted: French (France)

Formatted: French (France)

839 Gammon, P. H., Kieft, H., Clouter, M. J. and Denner, W. W.: Elastic constants of artificial and natural ice samples by Brillouin
840 spectroscopy, *Journal of Glaciology*, 29(103), 433-460, doi: 10.3189/S0022143000030355, 1983.

841 Gaume, J., van Herwijnen, A., Chambon, G., Birkeland, K. W., and Schweizer, J.: Modeling of crack propagation in weak
842 snowpack layers using the discrete element method, *The Cryosphere*, 9, 1915–1932. doi: 10.5194/tc-9-1915-2015, 2015.

843 Gaume, J., van Herwijnen, A., Chambon, G., Wever, N., and Schweizer, J.: Snow fracture in relation to slab avalanche release:
844 Critical state for the onset of crack propagation, *The Cryosphere*, 11(1), 217–228, doi: 10.5194/tc-11-217-2017, 2017.

845 [Gaume, J., Löwe, H., Tan, S., and Tsang, L.: Sacaling laws for the mechanics of loose and cohesive granular materials based
846 on Baxter's sticky hard spheres, *Physical Review E*, 96, 032914, doi: 10.1103/PhysRevE.96.032914, 2017.](#)

847 Gubler, H. U.: On the ramsonde hardness equation, *IAHS-AISH Publ.* 114, 110–121, 1975.

848 Gubler, H. U.: Determination of the mean number of bonds per snow grain and of the dependence of the tensile strength of
849 snow on stereological parameters, *J. Glaciol.* 20, 329–341, doi: 10.3189/S0022143000013885, 1978.

850 Hagenmuller, P., Chambon, G., Lesaffre, B., Flin, F., and Naaim, M.: Energy-based binary segmentation of snow
851 microtomographic images, *J. Glaciol.* 59 (217), 859–873, doi: 10.3189/2013JoG13J035, 2013.

852 Hagenmuller, P., Calonne, N., Chambon, G., Flin, F., Geindreau, C., and Naaim, M.: Characterization of the snow
853 microstructural bonding system through the minimum cut density, *Cold Reg. Sci. Technol.* 108, 72–79, doi:
854 10.1016/j.coldregions.2014.09.002, 2014.

855 Hagenmuller, P., Chambon, G., Flin, F., Morin, S., and Naaim, M.: Snow as a granular material: assessment of a new grain
856 segmentation algorithm, *Gran. Matter* 16 (4), 421–432, doi: 10.1007/s10035-014-0503-7, 2014.

857 Hagenmuller, P., Chambon, G., and Naaim, M.: Microstructure-based modeling of snow mechanics: A discrete element
858 approach, *Cryosphere*, 9(5), 1969–1982, doi: 10.5194/tc-9-1969-2015, 2015.

859 [Hansen, A. C. and Brown, R. L.: An internal state variable approach to constitutive theories for granular materials with snow
860 as an example, *Mech. Mater.*, 7, 109–119, doi: 10.1016/0167-6636\(88\)90009-9, 1988.](#)

861 Heggli, M., B. Köchle, M. Matzl, B. R. Pinzer, F. Riche, S. Steiner, D. Steinfeld, and M. Schneebeli: Measuring snow in 3-D
862 using X-ray tomography: Assessment of visualization techniques, *Ann. Glaciol.*, 52(58), 231–236,
863 doi:10.3189/172756411797252202, 2011.

864 Herwijnen, A. V.: Experimental analysis of snow micropenetrometer (SMP) cone penetration in homogeneous snow layers,
865 *Can. Geotech. J.* 50, 1044–1054. doi: 10.1139/cgj-2012-0336, 2013.

866 Jamieson, J. B., and Johnston, C. D.: Snowpack characteristics associated with avalanche accidents, *Canadian Geotechnical
867 Journal*, 29(5), 862–866, doi: 10.1139/t92-093, 1992.

868 Johnson, J., and Schneebeli, M.: Characterizing the microstructural and microchemical properties of snow, *Cold Reg. Sci.
869 Technol.* 30, 91–100. doi: 10.1016/S0165232X(99)00013-0, 1999.

870 Johnson, J. B. and Hopkins, M. A.: Identifying microstructural deformation mechanisms in snow using discrete-element
871 modeling, *J. Glaciol.*, 51, 432–442. doi: 10.3189/172756505781829188, 2005.

872 Kozak, M. C., Elder, K., Birkeland, K., and Chapman, P.: Variability of snow layer hardness by aspect and prediction using
873 meteorological factors, *Cold Regions Science and Technology*, 37(3): 357–371. doi:10.1016/S0165-232X(03)00076-4, 2003.

874 Lunne, T., Robertson, P. K., and Powell, J. J. M.: *Cone penetration testing in geotechnical practice*. Blackie Academic, EF
875 Spon/Routledge, New York, 1997.

876 LeBaron, A., Miller, D., and van Herwijnen, A.: Measurements of the deformation zone around a split-axis snow
877 micropenetrometer tip, *Cold Reg. Sci. Technol.* 97, 90–96. doi: 10.1016/j.coldregions.2013.10.008, 2014.

878 Lowe, H., and van Herwijnen, A.: A Poisson shot noise model for micropenetration of snow, *Cold Regions Science and*
879 *Technology*, 70: 62–70. doi: 10.1016/j.coldregions.2011.09.001, 2012.

880 McCallum, A.: A brief introduction to cone penetration testing (CPT) in frozen geomaterials, *Ann. Glaciol.* 55, 7–14. doi:
881 10.3189/2014 AoG68A005, 2014.

882 Mackenzie, R., and Payten, W.: A portable, variable-speed, penetrometer for snow pit evaluation, In *Proceedings of the 2002*
883 *International Snow Science Workshop*, Penticton, B.C. pp. 294–300, 2002.

884 Maeno, N. and Arakawa, M.: Adhesion shear theory of ice friction at low sliding velocities, combined with ice sintering,
885 *Journal of Applied Physics*, 95(1), 134-139, doi: 10.1063/1.1633654, 2004.

886 Marshall, H.P., and Johnson, J.B.: Accurate inversion of high-resolution snow penetrometer signals for microstructural and
887 micromechanical properties, *Journal of Geophysical Research: Earth Surface*, 114(F4): F04016. doi: 10.1029/2009JF001269,
888 2009.

889 Mede, T., Chambon, G., Hagenmuller, P., and Nicot, F.: A medial axis based method for irregular grain shape representation
890 in DEM simulations, *Granular Matter*, 20(1), 1-11, doi: 10.1007/s10035-017-0785-7, 2018a.

891 Mede, T., Chambon, G., Hagenmuller, P., and Nicot, F.: Snow failure modes under mixed loading, *Geophys. Res. Lett.* 45
892 (24), 13–351, doi: 10.1029/2018GL080637, 2018b.

893 Mede, T., Chambon, G., Nicot, F., and Hagenmuller, P.: Micromechanical investigation of snow failure under mixed-mode
894 loading, *International Journal of Solids and Structures*, 199, 95–108. doi:10.1016/j.ijsolstr.2020.04.020, 2020.

895 Montagnat, M., Löwe, H., Calonne, N., Schneebeli, M., Matzl, M. and Jaggi, M.: On the birth of structural and crystallographic
896 fabric signals in polar snow: A case study from the EastGRIP snowpack, *Frontiers in Earth Science*, 8:365.
897 doi:10.3389/feart.2020.00365, 2020.

898 Narita, H.: An experimental study on tensile fracture of snow, *Contribut. Inst. Low Temperat. Sci.* A32, 1–37, 1983.

899 Peinke, I., Hagenmuller, P., Chambon, G., and Roulle, J.: Investigation of snow sintering at microstructural scale from micro-
900 penetration tests, *Cold Reg. Sci. Technol.* 162, 43–55. doi: 10.1016/j.coldregions.2019.03.018, 2019.

901 Peinke, I., Hagenmuller, P., Andò, E., Chambon, G., Flin, F. and Roulle, J.: Experimental Study of Cone Penetration in Snow
902 Using X-Ray Tomography, *Front. Earth Sci.* 8:63. doi: 10.3389/feart.2020.00063, 2020.

903 Proksch, M., Löwe, H., and Schneebeli, M.: Density, specific surface area, and correlation length of snow measured by high-
904 resolution penetrometry, *J. Geophys. Res. Earth Surf.* 120, 346–362. doi: 10.1002/2014JF003266, 2015.

905 Reuter, B., Schweizer, J., and van Herwijnen, A.: A process-based approach to estimate point snow instability, *Cryosphere*, 9,
906 837–847. doi: 10.5194/tc-9-837-2015, 2015.

907 Reuter, B., Proksch, M., Löwe, H., Van Herwijnen, A., and Schweizer, J.: Comparing measurements of snow mechanical
908 properties relevant for slab avalanche release, *J. Glaciol.* 65, 55–67. doi: 10.1017/jog.2018.93, 2019.

909 Ruiz, S., Straub, I., Schymanski, S. J., and Or, D.: Experimental evaluation of earthworm and plant root soil penetration-cavity
910 expansion models using cone penetrometer analogs, *Vadose Zone J.* 15, 1–14. doi: 10.2136/vzj2015.09.0126, 2016.

911 Ruiz, S., Capelli, A., van Herwijnen, A., Schneebeli, M., and Or, D.: Continuum cavity expansion and discrete
912 micromechanical models for inferring macroscopic snow mechanical properties from cone penetration data, *Geophys. Res.*
913 *Lett.* 44, 8377–8386. doi: 10.1002/2017GL074063, 2017.

914 Shapiro, L.H., Johnson, J. B., Sturm, M., and Blaisdell, G. L.: Snow mechanics: review of the state of knowledge and
915 applications, CRREL Rep. 97-3, 1997.

916 Schaap, L. H. J. and Fohn, P. M. B.: Cone penetration testing in snow, *Canadian Geotechnical Journal* 24(3):335-341.
917 doi:10.1139/t87-044, 2011.

918 Schneebeli, M.: Numerical simulation of elastic stress in the microstructure of snow, *Annals of Glaciology*, 38. doi:
919 10.3189/172756404781815284, 2004.

920 Schneebeli, M., and Johnson, J. B.: A constant-speed penetrometer for high resolution snow stratigraphy, *Annals of*
921 *Glaciology*, 26: 107–111, doi: 10.3189/1998AoG26-1-107-111, 1998.

922 Schneebeli, M., and Sokratov, S. A.: Tomography of temperature gradient metamorphism of snow and associated changes in
923 heat conductivity, *Hydrol. Process.*, 18(18), 3655–3665, doi: 10.1002/hyp.5800, 2004.

924 Schulson, E. M. and Duval, P.: *Creep and Fracture of Ice*, Cambridge University Press, 2009.

925 Schweizer, J., Jamieson, J. B., and Schneebeli, M.: Snow avalanche formation, *Rev. Geophys.*, 41(4), 1016.
926 doi:10.1029/2002RG000123, 2003.

927 Šmilauer, V., Catalano, E., Chareyre, B., Dorofeenko, S., Duriez, J., Gladky, A., Kozicki, J., Modenese, C., Scholtès, L.,
928 Sibille, L., Stransky, J., and Thoeni, K.: Yade reference documentation. In V. Šmilauer (Ed.), *Yade Documentation* (Vol. 474).
929 Retrieved from <http://yadedem.org/doc>, 2010/

930 ~~Szabo, D. and Schneebeli, M.: Subsecond sintering of ice, *Applied Physics Letters*, 90, 151916, doi: 10.1063/1.2721391, 2007.~~

931 Thorsteinsson, T.: An analytical approach to deformation of anisotropic ice-crystal aggregates, *Journal of Glaciology*, 47
932 (158), 507–516, doi: 10.3189/172756501781832124, 2001.

933 Vionnet, V., Brun, E., Morin, S., Boone, A., Faroux, S., Le Moigne, P., Martin, E. and Willemet, J.-M.: The detailed snowpack
934 scheme Crocus and its implementation in SURFEX v7.2, *Geosci. Model Dev.*, 5, 773–791. doi: 10.5194/gmd-5-773-2012,
935 2012.

936 Wautier, A., Geindreau, C., and Flin, F.: Linking snow microstructure to its macroscopic elastic stiffness tensor: A numerical
937 homogenization method and its application to 3-D images from x-ray tomography, *Geophysical Research Letters*, 42, 8031–
938 8041. <https://doi.org/10.1002/2015GL065227>, 2015.

939 Yu, H. S., and Carter, J.: Rigorous similarity solutions for cavity expansion in cohesive-frictional soils, *Int. J. Geomech.*, 2,
940 233–258. doi:10.1061/(ASCE)1532-3641(2002)2:2(233), 2002.